Original article

Biochar derived from traditional Chinese medicine residues: An efficient adsorbent for heavy metal Pb(II)

Jiandan Yuan [a], Chengjiu Wang [a], Zhentao Tang [b], Tianzhe Chu [a], Chuan Zheng [c,*], Qingrong Han [a], Hulan Chen [a,b,*], Yuzhu Tan [a,*]

[a] Key Laboratory of Southwestern Chinese Medicine Resources, School of Pharmacy, Chengdu University of Traditional Chinese Medicine, Chengdu 611137, China
[b] College of Medical Technology, Chengdu University of Traditional Chinese Medicine, Chengdu 611137, China
[c] Sichuan Key Laboratory of TCM Regulating Metabolic Diseases, Affiliated Hospital of Chengdu University of Traditional Chinese Medicine, Chengdu 610075, China

ARTICLE INFO

ABSTRACT

Biochar (BC) is widely used in the remediation of soil and wastewater polluted by heavy metals, but there are few reports on the characteristics of biochar derived via pyrolysis from different traditional Chinese medicine residues (TCMRs). In this study, biochars were prepared by slow pyrolysis of five common Chinese medicine residues, namely, *Salvia miltiorrhiza* (DNS), *Ligusticum striatum* (CX), *Angelica sinensis* (DG), *Codonopsis pilosula* (DGS), and *Astragalus membranaceus* (HQ). The biochars were systematically investigated by determining their physicochemical properties and using common characterization techniques. The Spearman correlation matrix between factors was used to examine relationships between properties of different biochars. Batch adsorption experiments were carried out to investigate the adsorption characteristics of biochar on Pb(II) and the mechanisms involved. The results showed that the physicochemical properties and adsorption performance of biochar were related to the type of its pharmaceutical residue. Biochar produced from materials with higher lignin content showed a better adsorption of the heavy metal Pb(II). All biochars were alkaline, with yields ranging from 29.30 to 38.65 %, and the main structure comprised of mesopores and macropores. The FT-IR and Boehm experiments revealed that the various TCMR biochars contained comparable functional groups, but their content varied. XRD and TEM results show that all biochar is amorphous with a crystalline structure, with the surface dominated by cellulose crystals and graphitic carbon. The O/C ratio (<0.2) and H/C ratio (<0.6) of biochars suggested that it had a desirable half-life. The TGA results confirmed its stability in the environment. The results of mineral experiments confirm the enrichment of the mineral content of biochar during biomass pyrolysis. The biochars' adsorption kinetics followed pseudo-second-order models ($R^2 > 0.99$), and their isotherms were consistent with the Langmuir model ($R^2 > 0.99$), indicating a monolayer chemisorption process. The biochar samples exhibited varying adsorption capacities for Pb(II), with the highest capacity observed for B_{DNS} (36.42 mg/g). The adsorption mechanism mainly involved precipitation, complexation with oxygen-containing functional groups, and ion exchange. This study indicates that biochars from herbal residues exhibit promising potential for adsorbing heavy metal Pb(II), suggesting biochar production as a viable method for recycling herbal residues.

1. Introduction

With the popularity of healthy living and the need to respond to major public health events (e.g., new coronavirus epidemics), the demand for herbal medicines is increasing gradually. According to the latest statistics, the 2020 edition of the Chinese Pharmacopoeia includes 2,711 types of traditional Chinese medicines, which give rise to tens of millions of tonnes of TCMRs in China annually (Lu and Li, 2021; Tao et al., 2021). Disposal of the resulting waste has become a problematic issue for the industry, because residues of herbal medicines are produced in large quantities and are highly polluting. Unfortunately, there is a lack of effective recycling methods for TCMRs. Currently, common recycling methods for TCMRs include use as cultivation substrates (Yuan et al., 2021), extraction of further ingredients (Su et al., 2021; Wang et al., 2020), composting (Zhou et al., 2018a, 2018b), and utilization for renewable energy generation (Xi et al., 2021; Yu et al., 2021a, 2021b).

In practice, all these methods carry the risk of causing secondary environmental pollution. Considering the inherent characteristics of Chinese herbal materials, which are mostly rich in cellulose and lignin, and the fact that pyrolysis could enhance the immobilization of heavy metals in biomass to a greater extent (Hou et al., 2022), the production and application of BC can become a new choice for the adsorption and removal of toxic and hazardous elements in polluted wastewater and soil.

Biochar (BC) is a carbon-rich (carbon content of greater than 60 %) solid material with high aromaticity that is obtained by thermochemical conversion of biomass under oxygen-poor or anaerobic conditions (Wang et al., 2021). During pyrolysis, most of the K, Na, Ca, Mg, and plant micronutrients, as well as about half of the N and P, in the biomass feedstock can be retained in biochar (Laird et al., 2010). Recycling nutrients and reusing the resource can be achieved by placing the residue in the form of BC in the environment (Yu et al., 2019). In recent years, biochar has been widely used in the removal of heavy metal ions based on its adsorption properties. Various types of biochar such as sludge biochar (Deng et al., 2024), food waste biochar (Tian et al., 2023), orange peel biochar (Afolabi & Musonge, 2023), etc. have been used in the study of heavy metal removal from wastewater. In soil remediation, researchers have used Litchi wood biochar (Chen et al., 2023), wheat straw biochar (Wu et al., 2023), and rice straw biochar (Ahmed et al., 2023) to study the sequestration of heavy metals, and the experimental results have demonstrated the excellent heavy metal adsorption capacity of the materials. At present, most biochar is obtained from raw materials such as rice straw, maize straw, and tree bark, whereas research on the use of biochar from TCMRs is relatively limited. As traditional Chinese medicine resources are being extensively developed and utilized, the disposal of waste has become a challenging issue. In comparison with biochar from traditional agricultural crops, biochar from residues has the advantages of abundant surface functional groups, a large specific surface area, a rich pore structure and a high adsorption capacity (Liang et al., 2021). Moreover, in comparison with traditional agricultural wastes such as rice straw and wood, TCMRs are inherently nutrient-rich. Their addition can increase the contents of cellulose, hemicellulose, and most micronutrients in the target substrate, which may be more suitable for soil improvement. Biochars prepared from Chinese medicine residue are available choices as a low cost sorbent to reduce agrochemical pollution and a best way of recycling resources (Wei et al., 2020). The biochar feedstock has been shown to be the key factor affecting performance in comparison with the preparation conditions (e.g., the pyrolysis temperature) (Das et al., 2021b; Wang et al., 2015). However, systematic studies of biochars from different TCMR sources have currently not been reported. In recent years, Pb(II) has become a widespread environmental concern due to its carcinogenicity and toxicity, which can cause permanent and serious damage to the human respiratory, digestive and nervous systems (Yang et al., 2023). Therefore, this experiment was conducted for Pb(II) as a research object.

Overall, the aim of this study was to investigate various aspects of the physicochemical properties and characterisation of five common types of TCMR biochars through their preparation. They were used for the removal of the heavy metal Pb(II) from water and then the underlying mechanisms were elucidated with a view to assessing their potential value as heavy metal adsorbents. The specific objectives of this study were (1) to carry out a systematic comparative analysis of the physicochemical properties and characterisation of the five pristine biochars, (2) to investigate the removal effect of the TCMR biochars on Pb(II) in aqueous solution through kinetic and isothermal experiments and model fitting, and (3) to speculate on the mechanism of adsorption of the heavy metal Pb(II) on the TCMR biochars through the characterisation of the biochars before and after adsorption. The results of the study will provide an important reference for the use of TCMR biochars to remove toxic and harmful elements and improve environments polluted by heavy metals.

2. Materials and methods

2.1. Feedstock

The raw materials were herbal residues of Danshen (DNS) (*Salvia miltiorrhiza* Bunge), Chuanxiong (CX) (*Ligusticum striatum* DC), Danggui (DG) (*Angelica sinensis* (Oliv.) Diels), Dangshen (DGS) (*Codonopsis pilosula* (Franch.) Nannf.), and Huangqi (HQ) (*Astragalus membranaceus* (Fisch.) Bunge), all of which are well-known traditional Chinese medicines with high usage rates in China. The herbal residues were all obtained from Chengdu Xinfoy Traditional Chinese Medicine Co., Ltd (Sichuan province, China). Moreover, other unmentioned reagents of analytical purity were employed in this work. The ultrapure water produced by the laboratory water purification system (18.25 MΩ cm^{-1}, WBZ1001-UP) was applied to the preparation of all aqueous solutions.

2.2. Preparation of biochars

The five herbal residues (DNS, CX, DG, DGS, and HQ) were dried in a blast oven at 130 °C for 5 h. The residues were then pyrolysed in a tube furnace at 500 °C for 2 h under vacuum. After cooling to room temperature, the prepared biochars were collected and weighed to calculate the yield. The biochars were crushed to a particle size of 1–2 mm and sealed in brown reagent bottles with caps and were denoted as B_{DNS}, B_{CX}, B_{DG}, B_{DGS}, and B_{HQ}, respectively.

2.3. Analysis of biomass and biochar

In this study, the cellulose content of the residues was measured via oxidation with H_2SO_4 and $K_2Cr_2O_7$, the hemicellulose content of the residues was determined via hydrolysis with 2 M HCl (Liu et al., 2022), and the lignin content of the residues was measured using 72 % H_2SO_4 (Wang et al., 2019). The values of the pH and electrical conductivity (EC) of the biochars were measured using a pH meter (PHS-3C$^+$, Ark Technology, China) and a conductivity tester (CT-20, Lichen Technology, China), respectively. The method was as follows: 1 g biochar was weighed into a 50 mL centrifuge tube, and ultrapure water was added in a ratio of 1:20 (g:mL). After the mixture was fully shaken for 30 min, it was allowed to stand for 1 min to determine the pH and EC. The ash content was determined by continuous heating in a muffle furnace at 815 ± 1 °C for 2 h (Fristak et al., 2022). In order to observe the phase transition of the TCMRs at 500°C, the dregs were determined by simultaneous thermogravimetry and differential scanning calorimetry (TGA-DSC) (STD Q600, TA, USA), and the description of the procedure and the results are given in the supplementary file. The samples were heated from room temperature up to 1000 °C at a constant heating rate of 20 °C/min using a N_2 atmosphere and a flow rate of 20 mL/min.

The pH_{pzc} value was determined, i.e., the pH_{pzc} value corresponding to a charge of zero, before and after biochar formation (Manoharan et al., 2022; Tran et al., 2016). This was made as follows: 0.1 g biochar was mixed with 25 mL of 0.1 mol/L $NaNO_3$. The initial pH (pH_I) of the solution was adjusted to 2–12 by means of 1 M HNO_3 and 1 M NaOH. The solution was then shaken at 150 rpm for 4 h at room temperature and the equilibrium pH (pH_E) was recorded. When the pH before and after shocking was equal it was taken as pH_{pzc} of the corresponding sample. The surface morphological properties of the residues and biochars were observed by scanning electron microscopy (SEM) (Axio Imager M2 EVO10, ZEISS, Germany). Observe and analyse the disordered and crystalline carbon of biochars using transmission electron microscopy (TEM) (JEM 2100F, JEOL, Japan). Qualitative analysis of the surface functional groups of the biochars was performed in the wave number range of 400–4000 cm^{-1} by Fourier transform infrared (FT-IR) spectroscopy (Nicolet iS50, Thermo Scientific, USA). The amount of surface acidic groups such as carboxylic acids, lactones, and phenols on the surface was determined by Boehm titration method mentioned in the previous study (Boehm, 1994). The relationship between weight loss

and elevated temperature of biochars was determined by thermal gravimetric analysis (TGA) (TGA2, Mettler, Switzerland). The specific surface area of the samples was determined by the Brunauer–Emmett–Teller method, and the pore size of the materials and their total pore volume were calculated by the Barret–Joyner–Halenda (BJH) method using a physisorption instrument (JW-BK100, JWGB, China). X-ray diffraction (XRD) (Ultima IV, Rigaku, Japan) was used for the analysis of crystalline features in the different samples, which were then compared to the Joint Committee on Powder Diffraction Standards (JCPDS) standards. The carbonization information of biochar was determined by Raman spectroscopy (inVia, Ranishaw, UK).

For the five biochars that were obtained, the contents of carbon (C %), hydrogen (H%), nitrogen (N%), and sulfur (S%) were determined using an elemental analyzer (UNICUBE, Elementar, Germany), and the oxygen content (O%) was calculated using the subtraction method (O% = 100 % − [Ash% + C% + H% + N% + S%]) (Wang et al., 2023). The contents of sodium (Na), potassium (K), calcium (Ca), magnesium (Mg), and the heavy metal lead (Pb) were determined by inductively coupled plasma mass spectrometry (ICP-MS) (NexION 2000, PerkinElmer, USA). SEM energy-dispersive spectroscopy (EDS) (Sigma 300, ZEISS, Germany), FT-IR spectroscopy (Nicolet iS50, Thermo Scientific, USA), and X-ray photoelectron spectroscopy (XPS) (K-Alpha, Thermo Scientific, USA) were used to characterize the Danshen biochar before and after adsorption, and an adsorption mechanism was suggested. Here, the sample of FT-IR was prepared by mixing with KBr, and surface functional groups were measured spectroscopically by pressing the film and scanning at 4000–400 cm^{-1}.

2.4. Adsorption experiments on Pb(II)

In order to better understand the adsorption of Pb(II) by the materials, adsorption kinetics and adsorption isotherm experiments were carried out for the biochars. For the adsorption kinetics experiments, a background solution containing 0.01 M NaNO$_3$ was prepared to maintain the ionic strength. A standard solution of Pb(II) was diluted with the above-mentioned solution to obtain a Pb(II) solution with a concentration of 300 mg/L. Then 0.1 g biochar was weighed into a 50 mL centrifuge tube, to which 25 mL of the Pb(II) solution was added. The initial pH was adjusted to 5.0 ± 0.1 by adding a small amount of 1 M HNO$_3$ or NaOH dropwise. The reaction was carried out at room temperature (25℃) for a time range of 0–24 h, and the solution was then passed through 0.45 μm microporous filter membranes. The concentration of Pb(II) in the filtrate was determined using the Inductively Coupled Plasma-Optical Emission Spectrometer (ICP-OES) (Optima 7000DV, PerkinElmer, USA), and the amount of Pb(II) (mg/g) adsorbed on the biochar (Q_t) was calculated. To investigate how the material interacts with Pb(II), an adsorption isotherm experiment was set up. The initial concentration of the solution was set at 20–500 mg/L. 0.1 g of BC was mixed with 25 mL of heavy metal solution (with 0.01 mol/L NaNO$_3$ as background solution) and the reaction was kept at room temperature (25℃) for 12 h. At the end of the reaction, the same procedure was used to prepare samples and the results were obtained by ICP-OES.

By the following equation:

$$Q_t = \frac{(C_i - C_t)V}{m}\#$$ (1)

where, C_i (mg/L) and C_t (mg/L) are the initial and equilibrium Pb(II) concentrations, respectively, V (L) is the volume of the solution, and m (g) is the mass of biochar added.

The pseudo-first-order (2), pseudo-second-order (3) and Elovich (4) models were selected in turn to fit the adsorption kinetic data:

$$ln(Q_e - Q_t) = lnQ_e - K_1 t\#$$ (2)

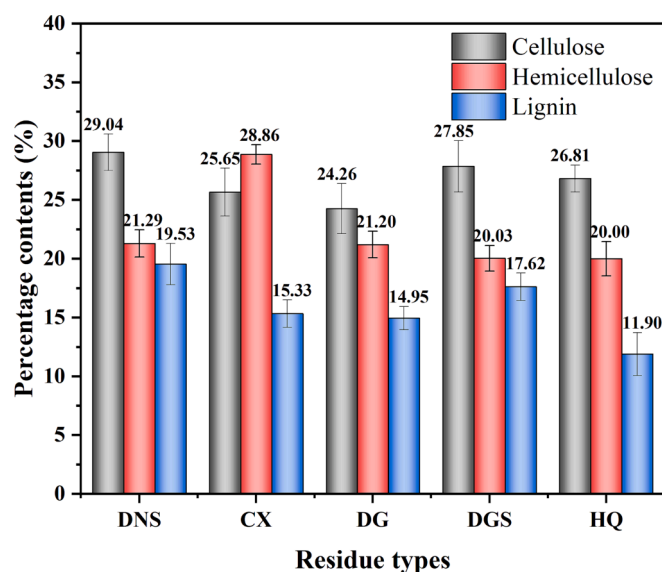$$\frac{t}{Q_t} = \frac{1}{K_2 Q_e^2} + \frac{t}{Q_e}\#$$ (3)

Fig. 1. The structure and composition of the TCMR biomasses.

$$Q_t = \frac{1}{\beta}ln(\alpha\beta) + \frac{1}{\beta}lnt\#$$ (4)

Where, Q_e and Q_t are the amount of Pb(II) adsorbed on BCs (mg/g) at equilibrium and at time t (min), respectively. K_1, K_2, α and β are fitting parameters.

The Langmuir (5) and Freundlich (6) models were selected in turn to fit the adsorption isotherms data.

$$\frac{C_e}{Q_e} = \frac{1}{K_L Q_m} + \frac{C_e}{Q_m}\#$$ (5)

$$ln(Q_e) = ln(K_f) + \frac{1}{n}ln(C_e)\#$$ (6)

Where, K_L and K_f are the fitting constants; Q_e is the equilibrium surface concentration (mg/g); Q_m is the maximum equilibrium surface concentration (mg/g); C_e is the equilibrium concentration in water (mg/L).

2.5. Statistical analysis

Differences between the residues and the biochars were compared by one-way analysis of variance and expressed as the least significant difference. A p-value of < 0.05 was considered to be statistically significant. Each treatment was repeated three times, and the results are shown as the mean values.

3. Results and discussion

3.1. Physicochemical properties

The weight, main constituents of the lignocellulosic materials and the thermal decomposition determines over the carbonaceous structure of the biochar (S & P, 2019). The carbon content, chemical structure, and ash content of the biochars varied according to the raw materials, which contained different proportions of cellulose, hemicellulose, and lignin (Song et al., 2019). The results showed that the cellulose content of the TCMR biochars ranged from 24.26 to 29.04 %, the hemicellulose content from 20.00 to 28.86 % and the lignin content from 11.90 to 19.53 %. The content was similar to that of straw-based biochar compared to the reported (S & P, 2019). Determination of the cellulose content showed that variations in lignocellulose composition occurred among the different medicine residues (Fig. 1). DNS had the highest
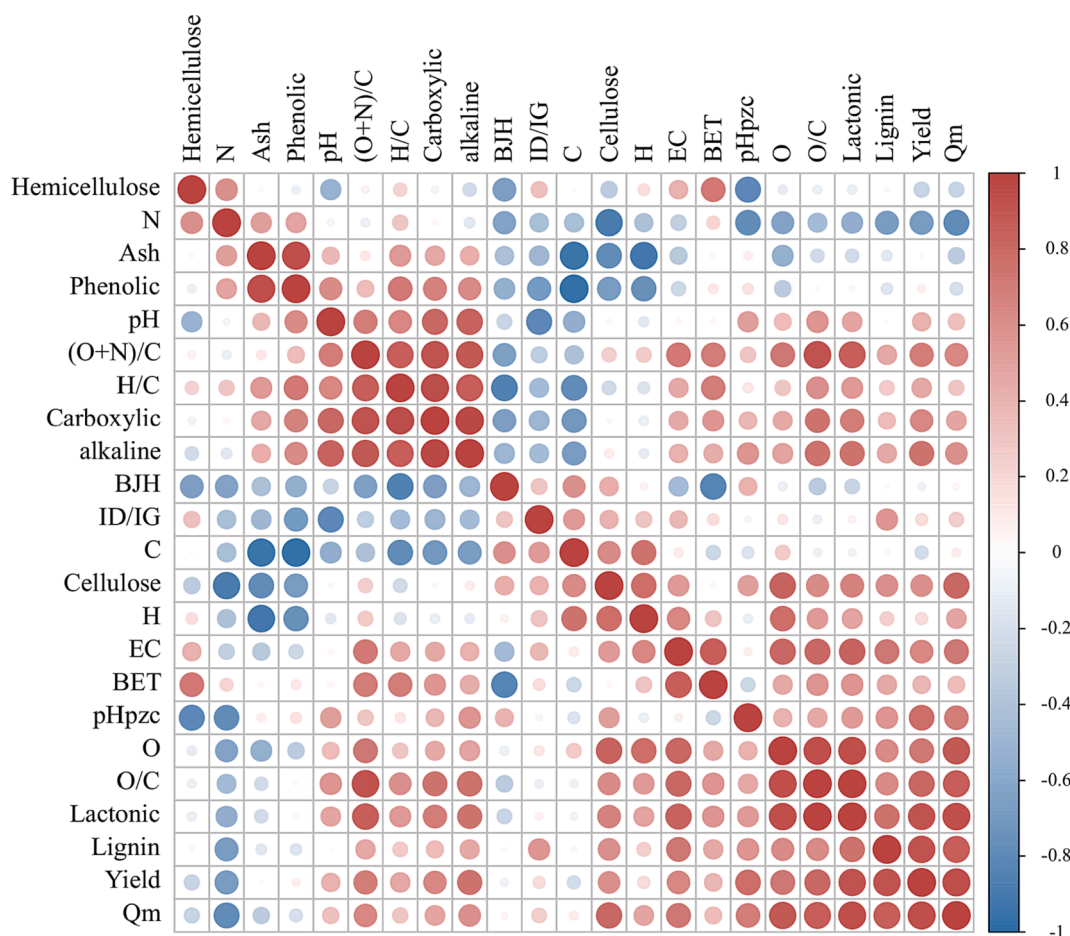
Fig. 2. The Spearman correlation matrix of physicochemical properties of the TCMR biochars.

Table 1
Basic physicochemical properties of the TCMR biochars.

Biochar	pH	EC (ms/cm)	Yield (%)	pH_{pzc}	SSA (m²/g)	PD (nm)	PV (cm³/g)
B_{DNS}	11.25	0.416	38.65	11.20	1.55	15.7942	0.0060
B_{CX}	10.04	0.334	30.45	8.06	1.60	11.7102	0.0043
B_{DG}	11.19	0.177	33.05	10.39	1.15	14.4215	0.0045
B_{DGS}	10.10	0.220	33.70	10.81	0.86	30.1202	0.0050
B_{HQ}	10.91	0.172	29.30	9.49	0.83	23.4360	0.0049

SSA specific surface area; PD pore diameter; PV pore volume.

lignin content (19.53 %), which corresponded to the highest yield (38.65 %). This was in accordance with findings in the literature that lignocellulosic biomass with a higher lignin content produces a higher biochar yield (Yaashikaa et al., 2019). A positive correlation (r = 0.90, p < 0.05) between biochar yield and lignin content was also found in our study (Fig. 2). Preliminary analysis of the basic properties of biochar obtained by pyrolysis showed that the physicochemical properties of biochars from different feedstocks varied considerably and that the properties of the biochar itself were the most important influencing factor (Zhao et al., 2023). This warrants further investigation.

As shown in Table 1, the pH values of the biochars after pyrolysis were all highly alkaline and reached 11.25 in the B_{DNS}. Pyrolysis would destroy some of the acidic functional groups of the biochar (e.g., carboxyl, hydroxyl, or carbonyl groups) in the early carbonization process, which would result in an increase in the pH of the biochar (Zhou et al., 2021a, 2021b, 2021c). The addition of biochar may influence the pH of soil, which plays a crucial role in the biological effects of heavy

metals in contaminated soil. An increase of 1 in the soil pH may result in a threefold increase in the binding ability of certain heavy metals (Beesley et al., 2011; Li et al., 2019b, 2019a; Mohamed et al., 2017). Furthermore, biochar has been shown to effectively adsorb metal cations, including Pb^{2+}, particularly at high pH values (Yaashikaa et al., 2019). Therefore, the application of biochar to soil has the potential to modify soil acidity and aid in the removal of heavy metals.

The EC values of the solutions containing biochar obtained from the residues indicated the concentrations of water-soluble ions. High EC values can have detrimental effects on crop growth in soil, such as reductions in water uptake and instability of nutrients (Das et al., 2021b). The EC values of the biochars were in the range of 0.172–0.416 mS/cm, and were thus overall at a low level that was ideal for use in soil.

The yields of the five biochars ranged from 29.30 % to 38.65 % (Table 1). These were similar to that of straw-based biochar (Sui et al., 2021), lower than the values of 40.2 %–91.1 % for sewage sludge biochar, and higher than those of most wood-based and animal manure biochars (Ghorbani et al., 2022). Since the pH of the medium can change the charcoal material and the adsorption charge, the pH_{pzc} should be taken into account in the adsorption process, especially when removing charged compounds such as heavy metals (Marzeddu et al., 2022). In this study, the pH_{pzc} values of the various biochars were measured, which demonstrated that the pyrolysis feedstocks had various effects on the surface of the resulting biochars (Fig. S1). It is worth noting that B_{CX} had the lowest pH_{pzc} value (8.06) among the five biochars, whereas B_{DNS} had the highest pH_{pzc} value (11.20). Owing to the continuous release of OH^- ions, the biochars were alkaline at the point of zero charge. Except for B_{DGS}, the pH values of the biochars were higher than their pH_{pzc} values. This indicated that the surface charge of the biochars was
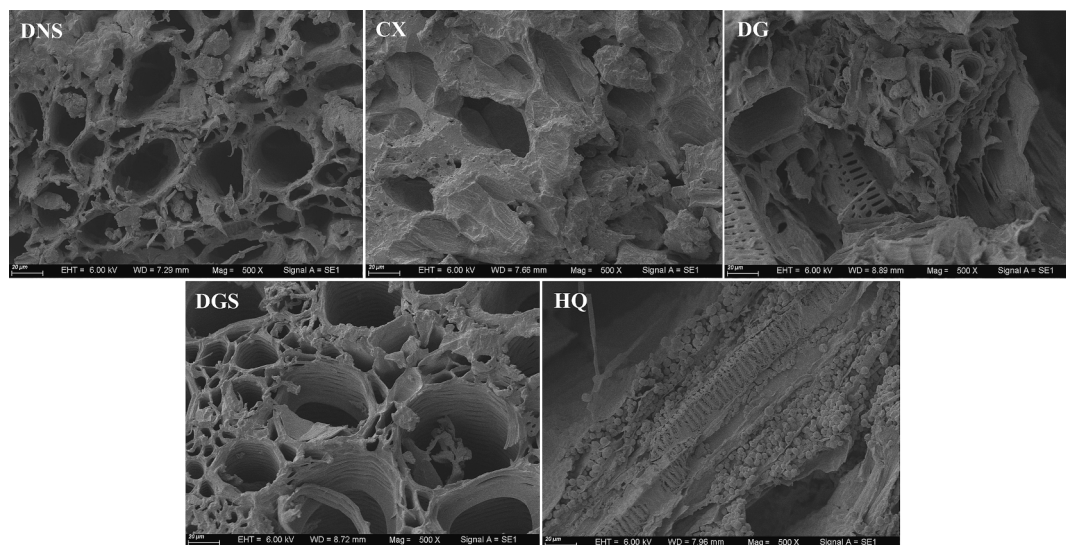
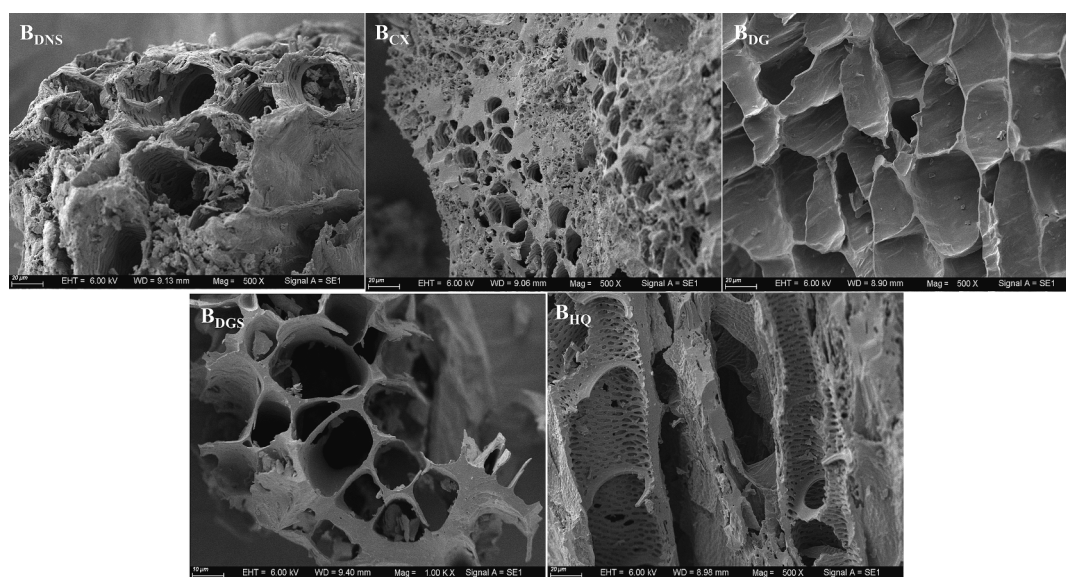**Fig. 3.** SEM images of the TCMR biomasses.

Fig. 4. SEM images of the TCMR biochars.

negative (Kim et al., 2021), which would facilitate the adsorption of cations by these materials.

To sum up, the above-mentioned excellent characteristics of TCMR biochars made it possible for them to be used as adsorbents for toxic and harmful substances (e.g., antibiotics, and heavy metals).

3.2. Characterization of biochars

3.2.1. SEM observations

Fig. 3 and Fig. 4 showed SEM images of the TCMR biomass feedstocks and biochars, respectively. There were distinct morphological differences among the feedstocks and biochars. In comparison with the TCMR feedstocks, the biochars contained obvious disordered pores, which might have been produced by the release of oxygenated volatiles from the biomass during pyrolysis (Jiang et al., 2022). In the case of B_{DNS}, the pores were more dispersed and some of the structure collapsed after pyrolysis, but the whole framework still had a good open texture. The raw material of CX was hard with a comparatively high density and fewer pores, but the overall appearance of the biochar after pyrolysis

was loose and porous. Structures such as the trapezoidal and reticulated channels and cork cells in DG and the xylem channels in DGS remained intact before and after thermal decomposition. At HQ, numerous powdery particles were adhered to the feedstock. After pyrolysis these particles disappeared, which exposed the pore structure on the surface. The biochars obtained from the five types of residues exhibited different surface morphologies, including both lamellar and porous structures. The unique channel-like structures of the residues themselves increased the surface area of the biochars (Ma et al., 2018), which was conducive to the adsorption of heavy metals.

Overall, the resulting biochars contained more loose pores than the residue feedstocks. Moreover, certain plant-specific structures such as cork cells and reticulated channels were preserved to some extent. This suggested that the pore structure of the feedstock can be retained in the thermally treated material, as previous studies have also indicated (Komkiene & Baltrenaite, 2015).

3.2.2. Structural features of biochars

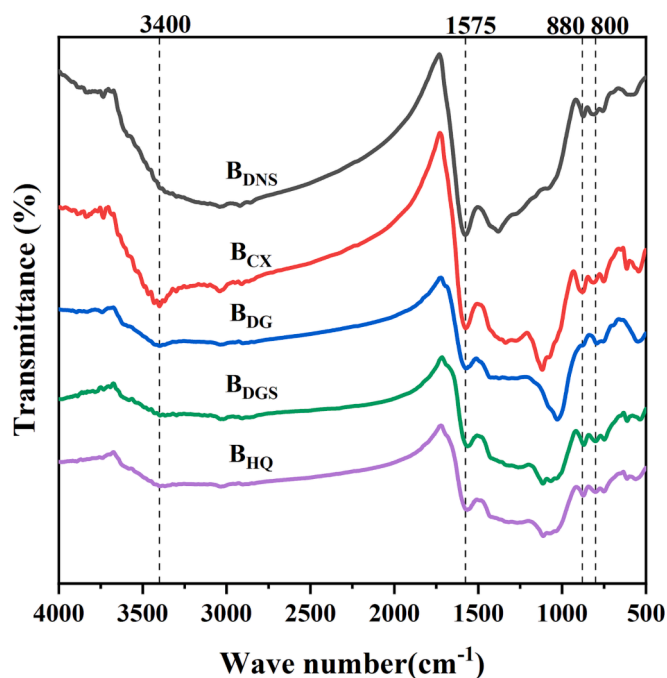In this study, all of the medicine residue biochars had a small specific

Fig. 5. The FT-IR spectrums of the TCMR biochars.

differs by almost sixty times between the two papers. The smaller one is only 0.84 m^2/g (Mehmood et al., 2022) and the larger one is 50.11 m^2/g (Fan et al., 2018). In addition, the specific surface area of biochar is also significantly affected by pyrolysis temperature. Biochar produced from the same wood mixture had a specific surface area of 3.54 m^2/g at 400℃, but when the pyrolysis temperature was increased to 700℃, the specific surface area was up to 220.41 m^2/g (Kalina et al., 2022). Meanwhile, literature reported that the adsorption performance of activated carbon (SSA = 1409 m^2/g) for Cu, Co and Pb was much lower than that of ten pristine biochar (SSA in the range of 1.05–5.41 m^2/g) (Huang et al., 2023). Regmi reported that commercially available powdered activated carbon (PAC) had very little affinity for copper and cadmium, even though its specific surface area was more than two orders of magnitude larger than that of switchgrass biochar (Regmi et al., 2012). This demonstrated that the heavy metal adsorption performance of a material was influenced by a number of factors, not just specific surface area. In this study, B$_{DNS}$ and B$_{CX}$ had relatively great advantages in terms of specific surface area (1.55–1.60 m^2/g) and had smaller average pore sizes (11.71–15.79 nm). If only the effect factor of specific surface area was considered, a large specific surface area and multiple pores can facilitate the physical pore filling of heavy metals in the removal process (Li et al., 2022). Therefore, B$_{DNS}$ and B$_{CX}$ have a greater potential to play a role if there is pore filling in the adsorption mechanism.

According to the International Union of Pure and Applied Chemistry classification, the adsorption/desorption isotherms for the five biochars conformed to the type III isotherm (Fig. S2), which proved the biochars were nonporous or macroporous materials. Based on the table of particle size distribution (Table S1), the prepared materials were mixtures of mesopores (2–50 nm) and macropores (>50 nm) materials. The isotherms were concave and had no inflection points. The amount of gas adsorbed increased with an increase in the partial pressures of the components. The isotherms also exhibited H$_3$-type (mesoporous) hysteresis loops with no obvious saturation plateau, which indicated that the biochars had uneven pore size distributions. In addition, the H$_3$-type hysteresis loops showed that the narrow pores created different

surface area (0.83–1.60 m^2/g) (Table 1). This was similar to the experimental results reported in the literature, where pristine biochar had a small specific surface area (Huang et al., 2023). Interestingly, the research found that the specific surface area of the different biochars varied particularly widely (0.82 to 420.30 m^2/g and 0.65 to 642 m^2/g, respectively) (Li et al., 2017; Liang et al., 2021). Furthermore, there are large differences in specific surface area between biochars produced from the same feedstock. For example, the specific surface area of rice straw biochar produced at the same pyrolysis temperature (500℃)
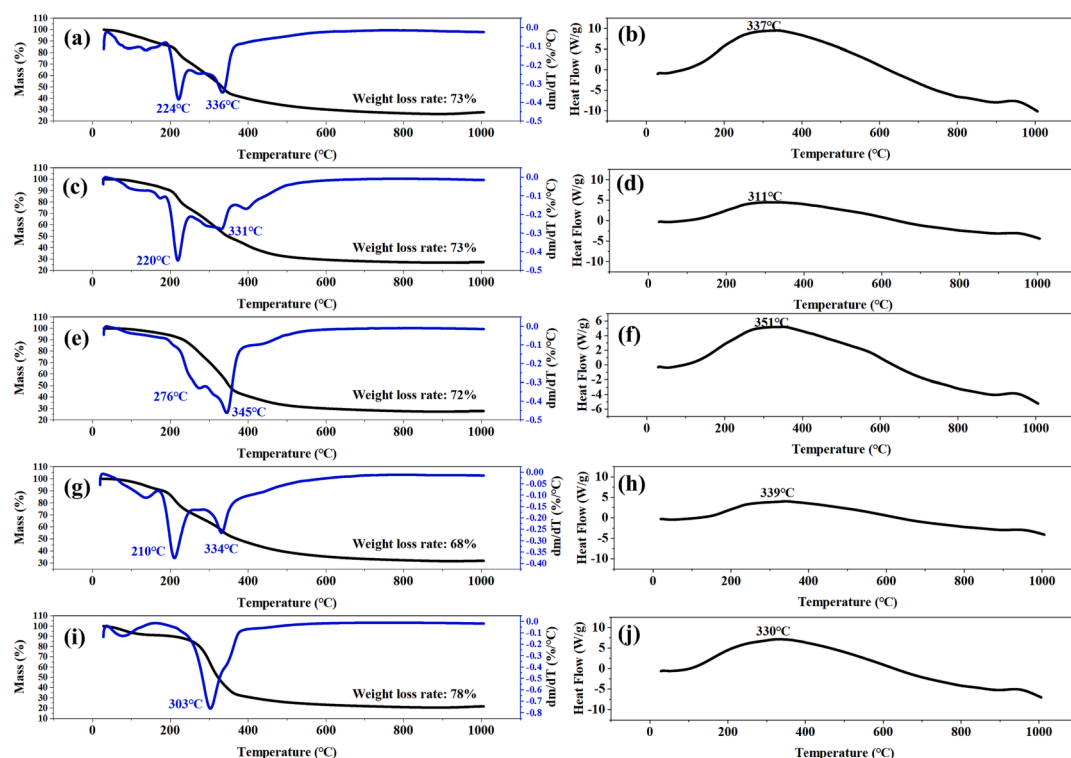

Fig. 6. TG-DTG and DSC curves of the TCMRs. (a, b) DNS; (c, d) CX; (e, f) DG; (g, h) DGS; (i, j) HQ.
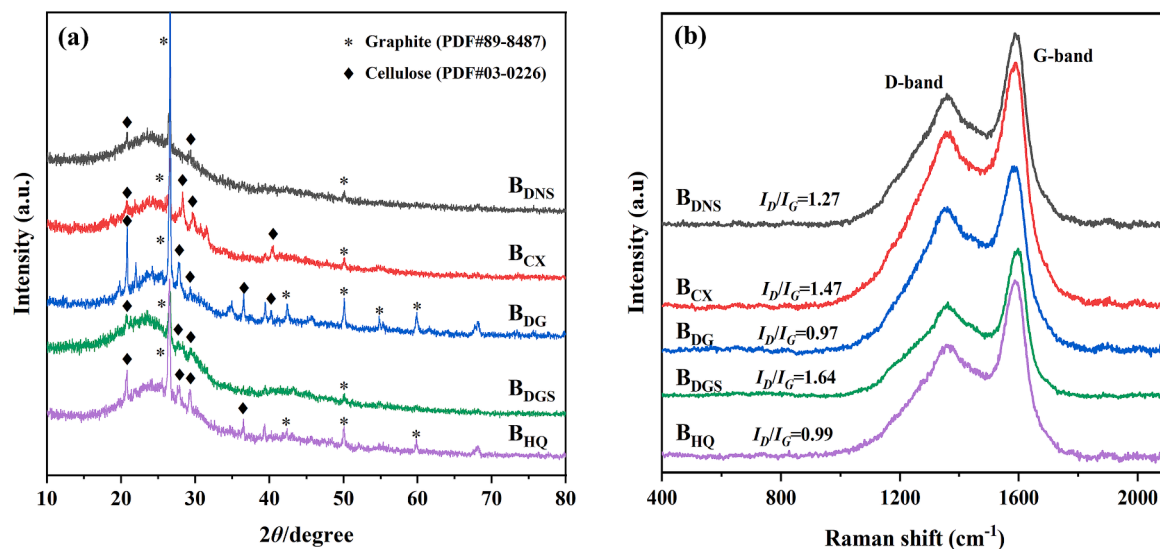
Fig. 7. (a) XRD patterns and (b) Raman spectra of the TCMR biochars.

pathways for the adsorption and desorption of N_2, which was consistent with the SEM images of the biochars (Mukome et al., 2013).

3.2.3. FT-IR spectroscopic analysis

The FT-IR spectra of surface functional groups in the five biochars were shown in Fig. 5, which indicated the presence of oxygen-, nitrogen-, and carbon-containing functional groups with peaks in the range of 400–4000 cm^{-1}. It could be seen that the types of surface functional groups in the biochars obtained from the five residues were mostly similar, with minor variations in band positions and wavenumbers and slight differences in the sharpness and intensity of peaks. Among the common peaks, the peak at 1575 cm^{-1} was attributed to COOH groups in carboxylic acids, the peak at 880 cm^{-1} was attributed to C–H or N–H out-of-plane bending, and the peak at 800 cm^{-1} was attributed to C–H bending in aromatic compounds (Hossain et al., 2011; Lu et al., 2013). In addition, different biochar materials gave rise to specific peaks. For example, the presence of alcoholic and phenolic hydroxyl groups in the biochars was indicated by the peak at 3400 cm^{-1}, which corresponded to the vibrations of OH groups in water molecules, alcohols, carboxylic acids, or metal hydroxides (Jin et al., 2016). This peak was most prominent in the spectrum of B_{CX}, whereas it was barely visible in those of B_{DNS} and B_{DGS}. The peak at 3040 cm^{-1} in the spectrum of B_{CX} was attributed to alkyl-CH_2 vibrations, and in the spectrum of B_{DNS} the peaks at 2920–2855 cm^{-1} were attributed to C–H stretching vibrations in CH_3 and CH_2 groups (Mukome et al., 2013). In the spectra of B_{DNS} and B_{CX} the peak at 1340 cm^{-1} was attributed to C-O/C-N stretching vibrations, and the peak near 1120 cm^{-1} was attributed to C-O stretching vibrations (Liu et al., 2017).

The results of FT-IR spectroscopy showed that the biochars obtained from the different plant residues had different types of functional groups on their surface. Combined with the results of the Boehm experiment (Table S2), it was found that the total amount of alkaline functional groups on the surface of biochar was higher than the total amount of acidic functional groups, which was a good explanation for the alkaline pH (Marzeddu et al., 2022). Meanwhile, the distribution of B_{DNS} functional groups showed relatively higher concentrations of carboxyl (0.15 mmol/g) and lactone groups (0.14 mmol/g) compared to the other biochars, which was consistent with the infrared spectra. In general, the presence of functional groups on the surface of biochar can provide an efficient means of removing heavy metals such as copper and cadmium through adsorption, chelation and precipitation reactions (Regmi et al., 2012). However, the specific removal effect is also influenced by factors such as the pore state of the biochar and the type and content of surface

functional groups. Further research is therefore required for practical applications. This demonstrated the potential adsorption capacity of these materials with respect to heavy metals and laid the foundation for further studies.

3.2.4. Phase transformation analysis

The thermal profiles of the dregs obtained from the simultaneous TGA-DSC analyser are shown in Fig. 6. The figure showed that the total mass loss remained around 70 % for all the TCMRs at 1000℃. Looking at the TGA-DTG curves, the mass loss (%) observed around 100℃ could initially be attributed to the loss of moisture on the surface of the TCMRs (Zhao et al., 2021). In addition, two distinct weight loss regions were found to exist in the ranges 210–276 °C and 331–345 °C respectively. The mass loss of the former peak was attributed to thermal degradation of hemicellulose, whereas the latter peak was associated with thermal degradation of cellulose, with an exothermic peak of cellulose located between 311 and 351 °C (Cappello et al., 2023; Zhang et al., 2020). This was due to the fact that the rigid structure of cellulose had a higher thermal stability than that of hemicellulose (Gonzalez-Canche et al., 2021). The DSC curves showed that the thermal equilibrium state was almost reached at the experimental condition of 500 °C, which was a more stable assessment of the state of the material.

Investigating the thermal stability of biochar is essential to achieve natural ageing resistance of the material (Zheng et al., 2023). In this experiment, TGA curves were used to determine the trend of physico-chemical properties of BC, mainly describing the weight loss versus temperature. Fig. S3 and Table S3 showed the TGA curves and weight loss of the TCMR biochars. The total weight loss was 18.22 % (B_{DNS}), 23.96 % (B_{CX}), 21.15 % (B_{DG}), 19.28 % (B_{DGS}) and 21.95 % (B_{HQ}), respectively. Among them, B_{DNS} and B_{DGS} showed a lower loss of mass, which indicated that these two biochars had a better thermal stability. From the thermal decomposition process, the thermal stabilisation stages of the four biochars, except B_{DGS}, were all three stages, presumably mainly due to the loss of water molecules (stage 1, around 100℃), thermal degradation of lignin (stage 2, around 600℃) and decomposition of other inorganic components (stage 3, around 900℃) (Gonzalez-Canche et al., 2021; Zhou et al., 2021a, 2021b, 2021c). For B_{DGS}, degradation of cellulose or hemicellulose was assumed to be responsible for the change at 322 °C. It has been reported in the literature that hemicellulose with an amorphous structure begins to degrade at 220℃, whereas cellulose, due to its highly stable crystalline structure, can be maintained at 300℃, followed by rapid weight loss at 315–400℃ (Dhyani & Bhaskar, 2018). The absence of this stage in other biochars
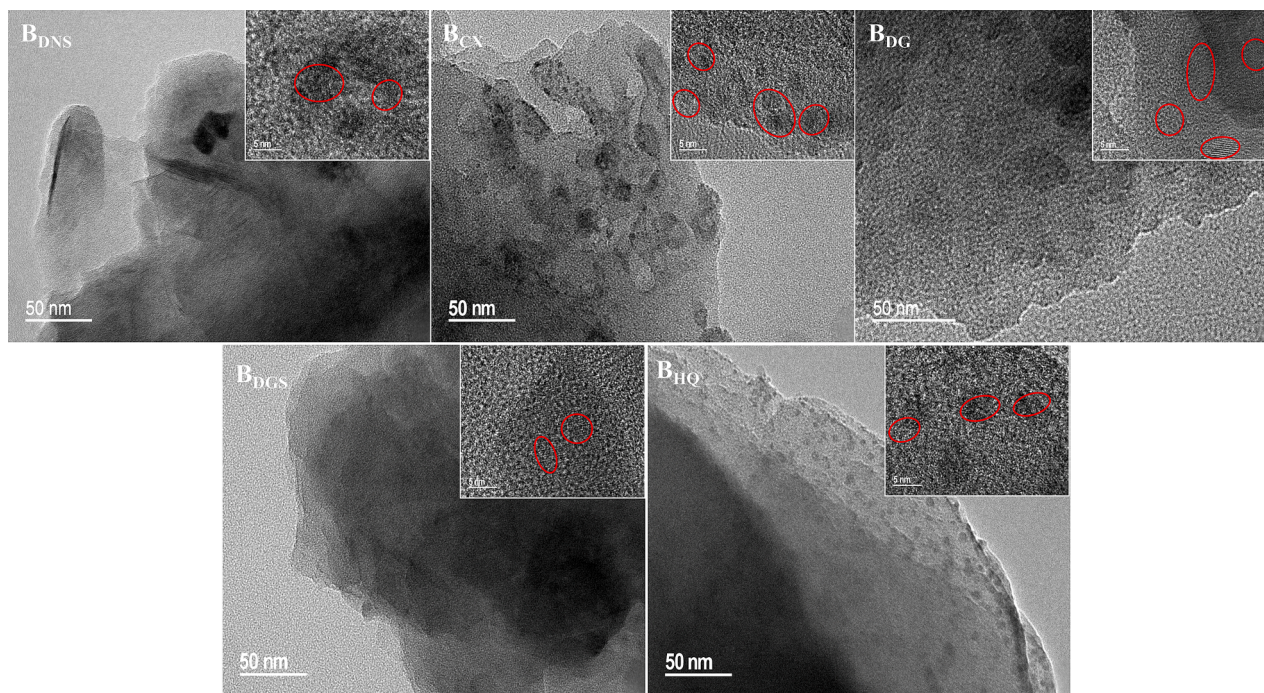
Fig. 8. TEM and HRTEM images of the TCMR biochars.

may be due to the fact that the hemicellulose is essentially completely pyrolysed and the cellulose partially pyrolysed at the preparation temperature of the biochar (500℃), which can be verified in the XRD section.

3.2.5. XRD patterns and TEM images of biochars

The structure and phase composition of BCs were shown in the XRD pattern (Fig. 7(a)). A long range disordered peak appeared on the XRD of all biochars in the 2θ range of 20°–30°, demonstrating the presence of amorphous structures on the material (Zhang et al., 2018). The XRD results showed that all biochars were amorphous structures with crystal structures (Das et al., 2021a). Common peaks belonging to graphite microcrystals were present on all biochars, mainly corresponding to several peaks at 2θ = 26.554°, 42.374°, 50.654° and 59.907° (Shao et al., 2021). The graphite microcrystalline peaks on B_{DG} and B_{HQ} were more numerous and sharper, indicating a higher degree of graphitisation than the other three biochars. The TEM and HRTEM results of the five biochars were shown in Fig. 8. B_{DNS} and B_{DGS} had smooth surfaces and contained some graphitic carbon layer structures with no microporous or mesoporous structures observed. In contrast, B_{CX} and B_{DG} had rough surfaces with obvious pore structures. B_{HQ} showed an outer layer with fine pores and a lamellar structure. The B_{DNS} and B_{DGS} surfaces were analysed by TEM and found to have an amorphous carbon layer distribution with some graphitic carbon layers. The graphitic structure results from the graphitisation and aromatisation of cellulose-type components in biomass (Hu et al., 2020). Among them, aromatisation facilitates the formation of cation-π interactions, which can improve the adsorption capacity of the materials for heavy metal cations (Zhou et al., 2022). From the above, it can be speculated that B_{DNS} and B_{DGS} have better adsorption potential for heavy metals. Meanwhile, the presence of lattice striations could be detected in the HRTEM images of all biochars. Combined with the analysis of the XRD results, this helped to verify the presence of crystalline carbon.

In addition, a large number of crystalline cellulose peaks were found on all biochars, corresponding to several peaks at 2θ = 20.639°, 27.593°, 29.454° and 36.649°, suggested that the cellulose in the TCMRs reacted to form crystals under pyrolysis conditions (Zhou et al., 2021a, 2021b, 2021c). This is consistent with literature reports that cellulose

conversion of biomass occurs during pyrolysis, resulting in carbon-rich amorphous biochar formed (Biswas et al., 2018; Kaur et al., 2023). This was also consistent with the results of the thermal stability experiments, where the hemicellulose was completely pyrolysed and cellulose was detected. In summary, it was speculated that the carbon material obtained in this experiment was in a structure where amorphous carbon and graphitised carbon coexisted.

3.2.6. Raman spectrum in biochars

The graphitic structure was also confirmed by Raman spectroscopy (Fig. 7(b)). It was possible to distinguish two main peaks detected at approximately 1360 and 1588 cm^{-1} (Table S4), which implied the point defect degree (D-band) and the graphitic structures (G-band). The characteristic D-band can be attributed to the presence of disorder in the graphene structure, whereas the G-band is due to the stretching band of the sp^2-hybridized carbon (Zhou et al., 2023). The Raman signals for lignin and cellulose have been reported in the literature to be between 1000 and 1700 cm^{-1} (Agarwal & Ralph, 1997). This was consistent with the characteristic peaks of cellulose in XRD. The intensity ratio between I_D and I_G reflects the degree of graphitisation. If this ratio is < 1, it indicates a high degree of graphitisation; if the ratio is > 1, it indicates the presence of a large number of functional groups on its surface (Marzeddu et al., 2022). Comparison of the magnitude of the I_D/I_G values showed that the values of B_{DG} (0.97) and B_{HQ} (0.99) were < 1, while the values of the other three biochars were > 1. This indicated that B_{DG} and B_{HQ} had a greater degree of graphitisation. This was consistent with the XRD results that more graphite microcrystals were present in B_{DG} and B_{HQ}. Meanwhile, more functional groups were present on the surfaces of B_{DNS}, B_{CX} and B_{DGS}, which could be favorable for adsorption of heavy metals.

As shown in Fig. 2, the correlation analysis of the I_D/I_G value with the physicochemical properties of biochar was investigated. It was found that this value does not correspond to a reliable correlation with any of the properties. This was consistent with literature reported that for biochar only, the peak or microcrystalline sizes obtained from different preparation processes did not correlate reliably with the O/C, H/C or C–C sp^2 of the material in XPS (Gabhi et al., 2020; Ilic et al., 2022).

Table 2
Ash and element content of the TCMR biochars.

Biochar	Ash(%)	C(%)	H(%)	N(%)	O(%)	S(%)	H/C	O/C	(O + N)/C
B_{DNS}	9.66	68.61	3.16	3.36	15.19	0.03	0.55	0.17	0.21
B_{CX}	12.04	70.54	3.03	4.84	9.25	0.30	0.52	0.10	0.16
B_{DG}	28.34	56.84	2.61	4.68	7.39	0.15	0.55	0.10	0.17
B_{DGS}	9.91	74.46	2.92	3.29	9.24	0.19	0.47	0.09	0.13
B_{HQ}	8.54	74.28	3.05	4.26	9.74	0.14	0.49	0.10	0.15

Table 3
Mineral elements and heavy metal contents of the TCMR biomasses.

Feedstock	Na(g/kg)	K(g/kg)	Ca(g/kg)	Mg(g/kg)	Pb(mg/kg)
DNS	0.84 ± 0.07[c]	13.64 ± 0.38[a]	0.43 ± 0.03[c]	4.60 ± 0.23[a]	1.72 ± 0.80[b]
CX	1.43 ± 0.40[ab]	12.88 ± 0.40[b]	0.64 ± 0.78[b]	2.45 ± 1.04[bc]	1.34 ± 0.16[b]
DG	1.57 ± 0.04[a]	7.04 ± 0.11[e]	1.40 ± 0.09[ab]	3.30 ± 0.12[b]	2.54 ± 0.14[a]
DGS	1.03 ± 0.06[bc]	11.89 ± 0.19[c]	0.28 ± 0.06[c]	1.65 ± 0.14[cd]	1.28 ± 0.11[b]
HQ	1.39 ± 0.07[ab]	7.63 ± 0.25[d]	0.23 ± 0.05[a]	1.29 ± 0.16[d]	1.07 ± 0.28[b]

The different letters in each column indicate significant differences between biochars from the various residues ($p < 0.05$).

Table 4
Mineral elements and heavy metal contents of five TCMR biochars.

Biochar	Na(g/kg)	K(g/kg)	Ca(g/kg)	Mg(g/kg)	Pb(mg/kg)
B_{DNS}	1.11 ± 0.13[c]	31.19 ± 2.02[b]	1.05 ± 0.07[b]	12.42 ± 0.40[a]	1.89 ± 0.27[b]
B_{CX}	2.20 ± 0.13[b]	37.21 ± 0.77[a]	0.74 ± 0.12[c]	5.98 ± 0.07[c]	1.96 ± 0.20[b]
B_{DG}	2.53 ± 0.26[ab]	20.10 ± 0.18[d]	3.40 ± 0.10[a]	7.87 ± 1.08[b]	4.07 ± 0.07[a]
B_{DGS}	1.43 ± 0.03[c]	31.66 ± 0.73[b]	0.89 ± 0.05[bc]	4.53 ± 0.17[d]	1.95 ± 0.15[b]
B_{HQ}	2.81 ± 0.29[a]	24.22 ± 0.24[c]	0.73 ± 0.11[c]	4.32 ± 0.29[d]	1.56 ± 0.05[b]

The different letters in each column indicate significant differences between biochars from the various residues ($p < 0.05$).

3.2.7. Structural elements in biochars

As shown in Table 2, the biochars obtained from the five different medicine residues varied considerably in terms of ash content. The ash content of B_{DG} was as high as 28.34 %, whereas the ash contents of B_{DNS}, B_{DGS}, and B_{HQ} did not vary much (8.54 %–9.91 %). The literature suggests that a higher ash content in the feedstock leads to a higher yield of biochar (Xiao et al., 2022). However, in this study a weak correlation (r = -0.01, $p < 0.05$) was observed between the ash content of the feedstock and the yield of biochar (Fig. 2), which could be attributed to the characteristics of the raw materials.

Elemental analysis showed that the carbon contents of the five biochars were mostly around 70 %, with B_{DG} having the lowest carbon content (56.84 %). The contents of both lignin (r = 0.63, $p < 0.05$) and cellulose (r = 0.84, $p < 0.05$) were positively correlated with the oxygen content, which also directly confirmed the positive proportional relationship between the contents of biochar components and the content of oxygen-containing functional groups. The stability of the biochars could be determined from the O/C and H/C ratios. The former ratio for all five biochars was less than 0.2, which indicated high stability with half-lives of greater than 1000 years (Ippolito et al., 2020). The H/C atomic ratio was maintained at around 0.5, and for all five biochars it was below the upper limit of 0.7. This indicated a larger, denser aromatic ring structure and that thermochemical transformations were occurring, which further

indicated the stability of the materials (IBI 2015). The lower is the H/C ratio, the higher is the aromaticity (Gao et al., 2019). The data indicated that B_{HQ} and B_{DGS} had slightly higher aromaticity than the other biochars. Furthermore, it is worth noting that the European Biochar Foundation (EBC) recommends biochar with an H/C ratio of less than 0.6 and an O/C ratio of less than 0.4 for effective carbon sequestration when applied to soil environments (EBC 2012). The results of the thermal stability of the biochar (weight loss ranging from 18.22 % to 23.96 %) are in agreement with the elemental analyses and O/C ratios related to the stability of the biochar (Fig. S3). As a result, the TCMR biochars have high stability in environmental treatment processes.

3.2.8. Mineral elements in biochars

Tables 3 and 4 showed the contents of four common mineral elements and a heavy metal in the TCMR feedstocks and biochars, respectively. A significant increase in the content of K by a factor of 2.29–3.17 times was observed in the biochars obtained by high-temperature preparation in comparison with the corresponding feedstocks. Moreover, the K content changed from 7.04 to 13.64 g/kg in the raw materials to 20.10–37.21 g/kg in the biochars, and the Na content changed from 0.84 to 1.57 g/kg in the raw materials to 1.11–2.81 g/kg in the biochars. This fully demonstrated that enrichment of mineral elements occurred when the TCMRs were converted into the biochars. The biochars exhibited higher contents of mineral elements than the raw materials. This indicated that a relative enrichment of each element occurred during pyrolysis, which was in accordance with previous findings in the literature (Xiao et al., 2022). Mineral constituents of biochar, such as potassium, calcium, and magnesium, have been reported in the literature to be beneficial for the adsorption of heavy metals in aqueous solutions (Duwiejuah et al., 2020). These mineral components and the heavy metals could be subjected to an ion exchange process, which would increase the binding affinity of the heavy metals on the surface of the biochar and greatly reduce their mobility (Lin et al., 2023a, 2023b; Mazarji et al., 2023), thus achieving the purpose of removing heavy metals.

In addition, the biochars in this study had high pH values, which was presumably due to the fact that most of the mineral elements were retained in the biochars after pyrolysis (Shi et al., 2019). In terms of mineral composition, the TCMRs and their biochars were richest in K (20.10–37.21 g/kg), followed by Mg (4.32–12.42 g/kg) (Table 4). With regard to individual residues before and after pyrolysis, DNS consistently had high levels of K and Mg, whereas DG had the highest Ca content. The Na contents of both DG and HQ were significantly different from those of the rest of the materials pre- and post-pyrolysis. Obviously, probably as a result of variations in the natural composition of the feedstocks, the mineral content of the biochars varied from one source to another (Mehmood et al., 2022; Shen et al., 2015).

Regarding the determination of heavy metal contents, there was little difference in the content of Pb(II) before and after pyrolysis, which proved that no enrichment of heavy metals occurred during pyrolysis of the herbal residues themselves and that there was no secondary pollution of the natural environment with heavy metals (Wu et al., 2016). Although the high K content of the biochars implies that they could act as part of a K fertilizer, potential damage to some K-sensitive plants needs to be considered.
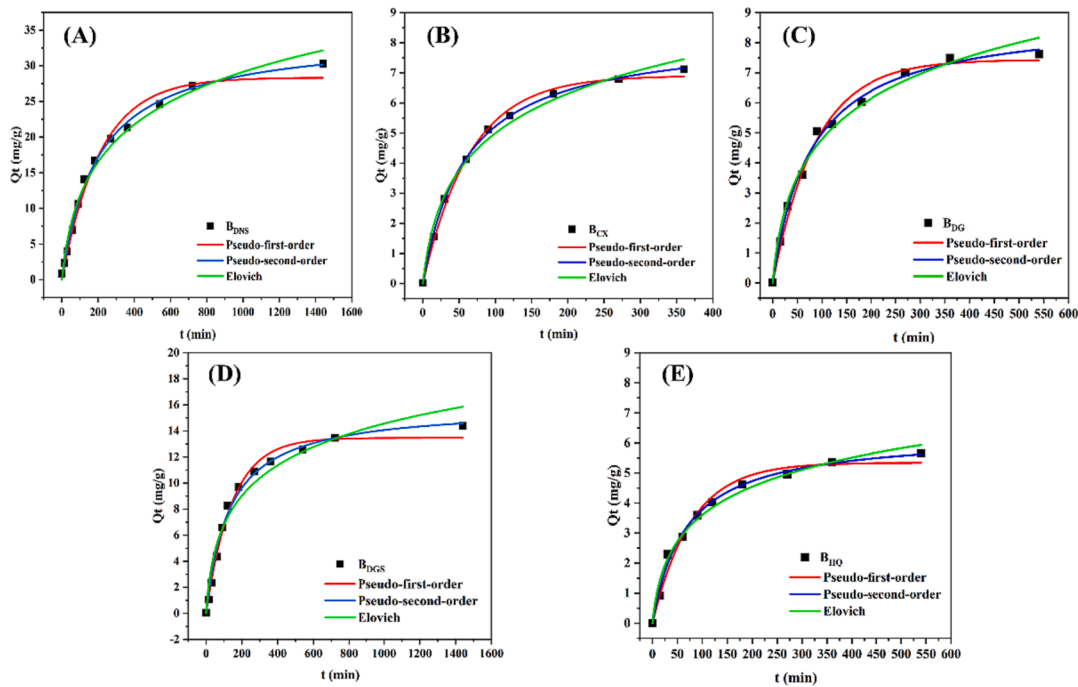
Fig. 9. Adsorption kinetic fitting curves of biochars. (A) Danshen (B) Chuanxiong (C) Danggui (D) Dangshen (E) Huangqi.

Table 5
Adsorption kinetic model parameters of the BCs for Pb(II).

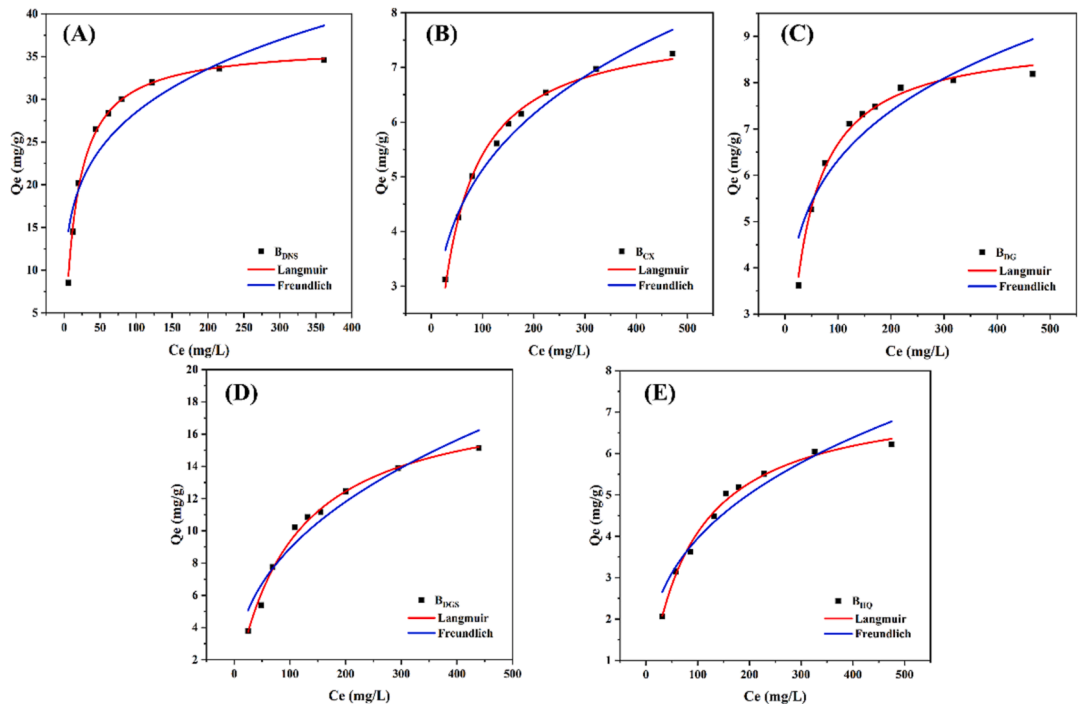| Biochar	Pseudo-first-order			Pseudo-second-order			Elovich		
	Q_e(mg/g)	K_1	R^2	Q_e(mg/g)	K_2	R^2	α	β	R^2
B_{DNS}	28.35	0.0047	0.9850	34.37	0.0001	0.9957	0.2545	0.1178	0.9857
B_{CX}	6.91	0.0153	0.9946	8.34	0.0020	0.9992	0.2196	0.4953	0.9881
B_{DG}	7.43	0.0114	0.9883	8.91	0.0014	0.9951	0.1827	0.4731	0.9845
B_{DGS}	13.47	0.0069	0.9893	15.91	0.0005	0.9923	0.2027	0.2780	0.9643
B_{HQ}	5.34	0.0129	0.9801	6.31	0.0024	0.9931	0.1614	0.6939	0.9842

Fig. 10. Adsorption isotherm fitting curves of biochars. (A) Danshen (B) Chuanxiong (C) Danggui (D) Dangshen (E) Huangqi.

Table 6
Adsorption isotherm model parameters of the BCs for Pb(II).

Biochar	Langmuir			Freundlich		
	Q_m(mg/g)	K_L(L/mg)	R^2	K_f	1/n	R^2
B_{DNS}	36.42	0.0582	0.9966	9.5354	0.2376	0.8381
B_{CX}	7.84	0.0222	0.9931	1.5394	0.2613	0.9439
B_{DG}	9.00	0.0289	0.9926	2.2521	0.2243	0.8453
B_{DGS}	18.67	0.0100	0.9914	1.3772	0.4055	0.9310
B_{HQ}	7.45	0.0122	0.9919	0.8029	0.3461	0.9194

### 3.3. Heavy metal removal

3.3.1. Pb(II) adsorption experiment

Fig. 9 showed the adsorption kinetic curves of five TCMR biochars and their fitted models. The whole adsorption process was divided into two steps: rapid adsorption and equilibrium adsorption. It is clear that all five biochars reached the equilibrium concentration at the experimental setting time (t = 720 min). By analysing the non-linear fit parameters of the pseudo-first-order and pseudo-second-order models (Table 5), the correlation coefficients of the pseudo-second-order models for all biochars with $R^2 > 0.99$ were higher than those of the pseudo-first-order models, indicating that the pseudo-second-order models were more consistent with the adsorption process of the original biochars. This suggested that chemisorption is the main adsorption process (Lin et al., 2023a, 2023b). The Elovich model, on the other hand, had a correlation coefficient $R^2 > 0.95$, indicating that the adsorption process included inhomogeneous phase diffusion (Zhou et al., 2022). The adsorption isotherms of biochars (Fig. 10) showed that the Langmuir correlation coefficient $R^2 > 0.99$, indicating that it was more consistent to be used to describe the adsorption behaviour of biochars. It indicated that the adsorption of biochars belonged to a monolayer adsorption process, where each active site on the adsorption surface had the same adsorption energy (Manoharan et al., 2022). The adsorption capacities of these five biochars were calculated by the Langmuir

isotherm model and were 36.42 mg/g (B_{DNS}), 7.84 mg/g (B_{CX}), 9.00 mg/g (B_{DG}), 18.67 mg/g (B_{DGS}), and 7.45 mg/g (B_{HQ}), respectively (Table 6). Although all the prepared biochars were able to remove Pb(II) from the solution, their adsorption capacities varied and depended on their individual properties. This was in accordance with been reported in the literature, which showed that different biochars obtained from different TCMR sources exhibited differences in sorption performance for heavy metals (Das et al., 2021a; Ding et al., 2017). The correlation between the amount of adsorption and the physicochemical properties of biochars was analysed (Fig. 2). It was found that the amount of adsorption (Qm) of biochar was strongly and positively correlated with the cellulose (r = 0.82, $p < 0.05$) and lignin (r = 0.87, $p < 0.05$) of the feedstock, as well as the oxygen content (r = 0.90, $p < 0.05$). However, adsorption showed a weak positive correlation with the pH_{pzc} (r = 0.71) and EC values (r = 0.73) of the materials. The differential contribution of the physicochemical properties of the materials to the effect of their adsorption performance was demonstrated. Among them, the adsorption properties of B_{DNS} and B_{DGS} were higher than those of several other biochars. This may be attributed to the high cellulose and lignin content and the associated specific physico-chemical properties, including conductivity, isoelectric point and other factors favourable to enhanced Pb(II) adsorption (Alcaniz-Monge et al., 2022; Li et al., 2020). In order to compare the sorption performance of the studied biochars, a review of literature was done about the biochars in other studies used for adsorping Pb(II) (Table S5). In contrast, B_{DNS} and B_{DGS} had relatively high adsorption capacities, and the other three had less satisfactory adsorption performance. In addition, further modification of the original biochar was required to enhance its adsorption performance and make it more effective in removing heavy metals from the environment. This is a challenge that the research group is currently addressing.

3.3.2. Pb(II) adsorption mechanism

In order to further elucidate the mechanism of the adsorption of Pb (II) by pristine biochar, experiments were carried out on B_{DNS}, and three
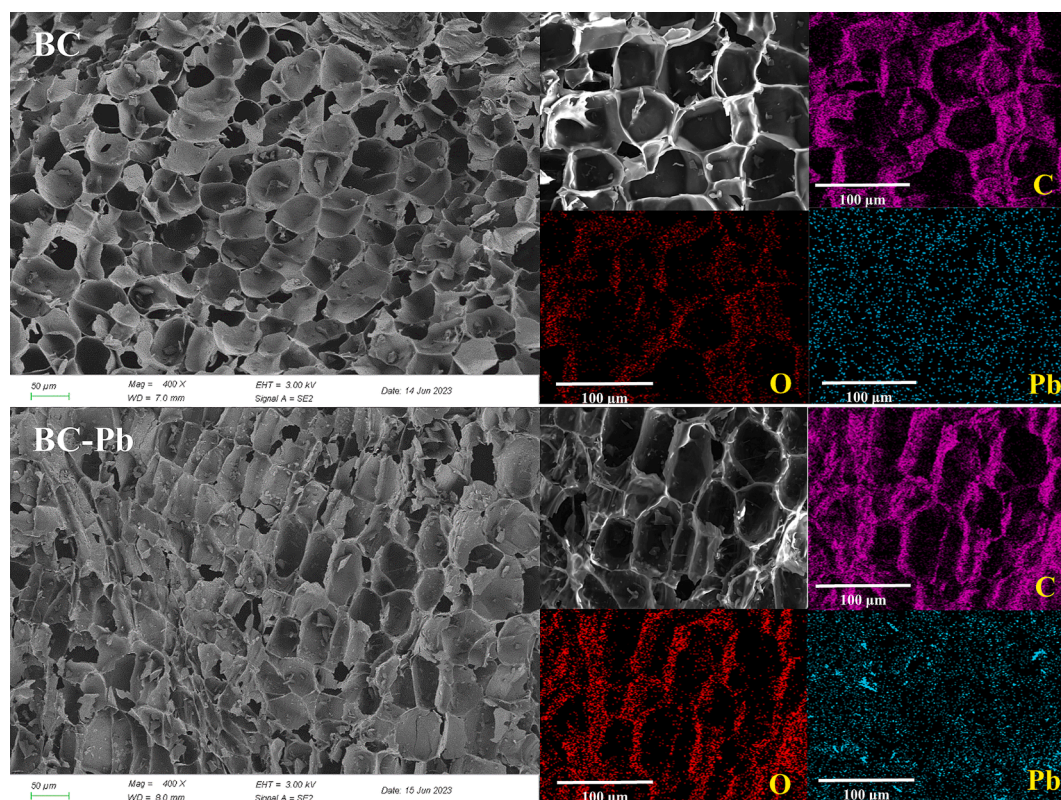
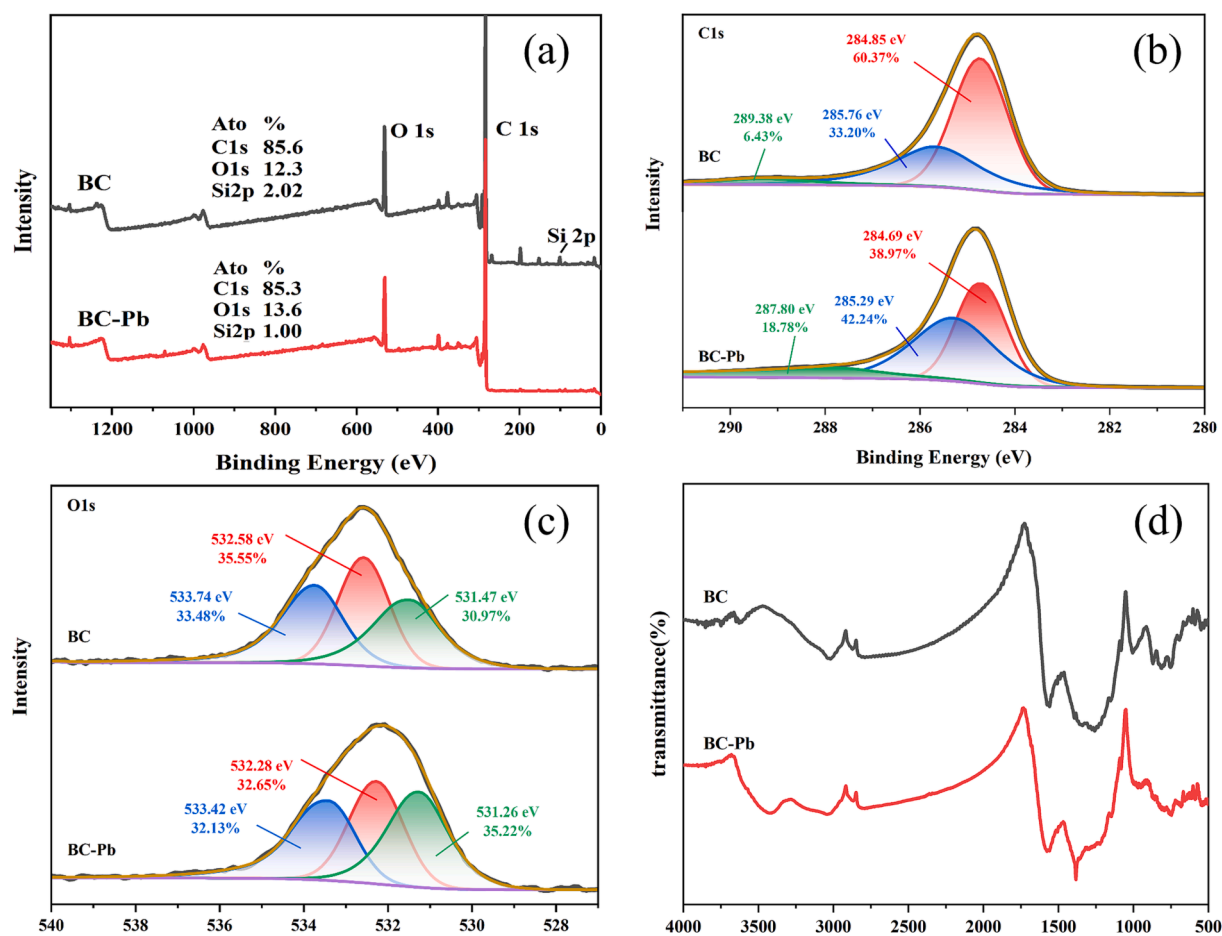**Fig. 11.** The SEM-EDS images of biochars before and after adsorption.

Fig. 12. The spectra of (a) XPS; (b) C 1 s; (c) O 1 s and (d) FT-IR including biochars before and after adsorption.

types of characterization, namely, SEM-EDS, FT-IR spectroscopy, and XPS, were performed before and after adsorption (Fig. 11 and Fig. 12). As shown in Fig. 11, uniformly distributed Pb(II) was visible on the surface of the biochar after adsorption, which demonstrated the successful adsorption of Pb(II). The semi-quantitative results using EDS show that Pb(II) increased by 5 % from the original 0 % (Fig. S4). Moreover, in comparison with the biochar before adsorption, many small particles appeared on the surface of the biochar after adsorption, which were presumed to consist of Pb(II)-related compounds that were generated.

Fig. 12(a–c) showed the XPS spectra of the biochar before and after the adsorption of Pb(II), which contained similar characteristic C 1 s and O 1 s peaks. From the semi-quantitative results, it was found that there was a clear silicon-related peak after adsorption, and the content of elemental silicon decreased from 2.02 % to 1.00 %, which demonstrated the involvement of silicon in the adsorption process. The literature reports that silicates can react with lead to form silicate precipitates (Li et al., 2019b, 2019a). The adsorption mechanism was further suggested by the high-resolution XPS spectra of C 1 s and O 1 s. The C 1 s peaks located at 284.8 eV (60.37 %), 285.7 eV (33.20 %) and 289.4 eV (6.43 %) were attributed to C–C/C–H/C = C, C-O/C-N, and C(=O)–OH groups, respectively (Das et al., 2023). After the adsorption of Pb(II), the percentage area of the C–C/C–H/C = C peak decreased from 60.37 % to 38.97 %, whereas the percentage area of C-O/C-N and C(=O)–OH peaks increased to 42.24 % and 18.78 % respectively. This may have been due to complexation or precipitation with Pb(II) resulted in the loss or gain of C in different valence states. Similarly, in the fine spectrum of O 1 s, the peaks located at 531.5 eV (30.97 %), 532.6 eV (35.55 %), and 533.7 eV (33.48 %) were attributed to C-OH, C = O, and O = C-OH(R) groups, respectively (Das et al., 2023; Herath et al., 2021). In the case of Pb(II)-loaded biochar, the percentage of peak area of C-OH increased from 30.97 % to 35.22 % and the percentage of C = O and O = C-OH(R) decreased to 32.65 % and 32.13 %, respectively. This may have been due to interactions between the groups and Pb(II). According to the various XPS peaks, different functional groups may have different adsorption capacities for heavy metals, with hydroxyl and carboxyl groups exhibiting higher adsorption capacities for Pb(II) (Yu et al., 2021a, 2021b).

According to the results of FT-IR mapping (Fig. 12(d)), after adsorption the two peaks at 1260 cm^{-1} and 1575 cm^{-1} appeared to be significantly weaker. These were attributed to C-O-C and COOH stretching vibrations, respectively (Li et al., 2019b, 2019a). The peak at 3440 cm^{-1}, which was attributed to O–H vibrations, appeared after the adsorption of Pb(II) by the biochar. This could be attributed to the introduction of Pb(II), which changed the functional groups on the biochar (Zhou et al., 2022). These changes suggested that oxygen-containing functional groups were utilized by Pb(II) and played an important role in the adsorption process. Moreover, abundant mineral elements (K, Ca, Na, and Mg) on the surface of the biochar could be exchanged with metal ions (Lin et al., 2023a, 2023b). The pH$_{pzc}$ of B$_{DNS}$ was higher than the initial pH of the solution and the adsorption capacity should be lower due to electrostatic attraction, whereas the adsorption capacity of B$_{DNS}$ was better, indicating that electrostatic attraction was not the main adsorption mechanism of B$_{DNS}$ (Zhou et al., 2018a, 2018b).

In conclusion, the adsorption mechanism mainly involved precipitation, complexation of oxygen-containing functional groups, and ion exchange to complete the process.

4. Conclusions

The biochars were systematically investigated by determining their physicochemical properties and using conventional characterization techniques. The relationships between properties of the different TCMR biochars were examined using the Spearman correlation matrix between influencing factors. The scientific validity of the preparation conditions and the stability of the material were demonstrated by studying the pyrolysis process and thermal stability. Additionally, the potential of biochar for adsorbing heavy metal Pb(II) and its related mechanisms were experimentally investigated. The results indicated that the adsorption process was consistent with pseudo-secondary kinetics and belonged to the chemisorption process. The isotherms were consistent with the Langmuir model. The biochar samples exhibited varying adsorption capacities for Pb(II), with the highest capacity observed for B_{DNS} (36.42 mg/g), followed by B_{DGS} (18.67 mg/g), B_{DG} (9.00 mg/g), B_{CX} (7.84 mg/g), and B_{HQ} (7.45 mg/g). This maximum adsorption capacity of 36.42 mg/g for Pb(II) is comparable to that of other pristine carbonaceous materials used in wastewater remediation processes. The enhanced adsorption of Pb(II) may be attributed to the richer cellulose, lignin, oxygen content, and the number of surface functional groups. The adsorption mechanism mainly involved precipitation, complexation with oxygen-containing functional groups, and ion exchange. The potential value of TCMR biochars in the adsorption of heavy metal Pb(II) was thus demonstrated.

In the future, three areas of follow-up research will be considered. Firstly, to improve the adsorption performance, it is necessary to modify the preparation process of raw biochars for different application environments, such as wastewater or soil. This will allow for its use in various forms in practice, such as adsorption columns, filtration membranes and biochar-based fertilisers. To improve the effectiveness of mixed heavy metal pollution treatment, it is necessary to expand the study of individual heavy metals to include other types. Furthermore, considering the physicochemical properties of the TCMR biochars, it may be possible to expand its applications by conducting adsorption studies on organic pollutants, including antibiotics. In conclusion, this study shows that biochars produced from herbal residues have good potential for the adsorption of heavy metal Pb(II) and that biochar production is a promising method for the recycling of herbal residues.

CRediT authorship contribution statement

Jiandan Yuan: Methodology, Writing – original draft, Visualization. **Chengjiu Wang:** Methodology, Resources. **Zhentao Tang:** . **Tianzhe Chu:** . **Chuan Zheng:** . **Qingrong Han:** . **Hulan Chen:** . **Yuzhu Tan:** Conceptualization, Supervision, Writing – review & editing.

Declaration of competing interest

The authors declare that they have no known competing financial interests or personal relationships that could have appeared to influence the work reported in this paper.

Acknowledgements

Appendix A. Supplementary data

Supplementary data to this article can be found online at https://doi.org/10.1016/j.arabjc.2024.105606.

References

Afolabi, F.O., Musonge, P., 2023. Synthesis, characterization, and biosorption of Cu(2+) and Pb(2+) ions from an aqueous solution using biochar Derived from Orange peels. Molecules 28 (20). https://doi.org/10.3390/molecules28207050.

Agarwal, U.P., Ralph, S.A., 1997. FT-raman spectroscopy of wood: identifying contributions of lignin and carbohydrate polymers in the Spectrum of black spruce (picea Mariana). Appl. Spectrosc. 51 (11), 1648–1655. https://doi.org/10.1366/0003702971939316.

Ahmed, W., Mehmood, S., Mahmood, M., Ali, S., Núñez-Delgado, A., Li, W., 2023. Simultaneous immobilization of lead and arsenic and improved phosphorus availability in contaminated soil using biochar composite modified with hydroxyapatite and oxidation: findings from a pot experiment. Environ. Res. 235, 116640 https://doi.org/10.1016/j.envres.2023.116640.

Alcaniz-Monge, J., Roman-Martinez, M.D.C., Lillo-Rodenas, M.A., 2022. Chemical activation of lignocellulosic precursors and residues: what Else to consider? Molecules 27 (5). https://doi.org/10.3390/molecules27051630.

Beesley, L., Moreno-Jimenez, E., Gomez-Eyles, J.L., Harris, E., Robinson, B., Sizmur, T., 2011. A review of biochars' potential role in the remediation, revegetation and restoration of contaminated soils. Environ. Pollut. 159 (12), 3269–3282. https://doi.org/10.1016/j.envpol.2011.07.023.

Biswas, B., Singh, R., Kumar, J., Singh, R., Gupta, P., Krishna, B.B., Bhaskar, T., 2018. Pyrolysis behavior of rice straw under carbon dioxide for production of bio-oil. Renew. Energy 129, 686–694. https://doi.org/10.1016/j.renene.2017.04.048.

Boehm, H.P., 1994. Some aspects of the surface chemistry of carbon blacks and other carbons. Carbon 32 (5), 759–769. https://doi.org/10.1016/0008-6223(94)90031-0.

Cappello, M., Rossi, D., Filippi, S., Cinelli, P., Seggiani, M., 2023. Wood residue-derived biochar as a low-cost, lubricating filler in poly(butylene succinate-co-adipate). Biocomposites. Materials (basel) 16 (2). https://doi.org/10.3390/ma16020570.

Chen, X., Jiang, S., Wu, J., Yi, X., Dai, G., Shu, Y., 2023. Three-year field experiments revealed the immobilization effect of natural aging biochar on typical heavy metals (pb, cu, cd). Sci. Total Environ. 912, 169384 https://doi.org/10.1016/j.scitotenv.2023.169384.

Das, S.K., Ghosh, G.K., Avasthe, R., Sinha, K., 2021a. Morpho-mineralogical exploration of crop, weed and tree derived biochar. J. Hazard. Mater. 407, 124370 https://doi.org/10.1016/j.jhazmat.2020.124370.

Das, S.K., Ghosh, G.K., Avasthe, R.K., Sinha, K., 2021b. Compositional heterogeneity of different biochar: effect of pyrolysis temperature and feedstocks. J. Environ. Manage. 278 (Pt 2), 111501 https://doi.org/10.1016/j.jenvman.2020.111501.

Das, N.K., Navarathna, C.M., Alchouron, J., Arwenyo, B., Rahman, S., Hoffman, B., Lee, K., Stokes, S., Anderson, R., Perez, F., Mohan, D., Pittman Jr., C.U., Mlsna, T., 2023. Efficient aqueous molybdenum removal using commercial Douglas fir biochar and its iron oxide hybrids. J. Hazard. Mater. 443 (Pt B), 130257 https://doi.org/10.1016/j.jhazmat.2022.130257.

Deng, S., Ren, B., Hou, B., Deng, X., Deng, R., Zhu, G., Cheng, S., 2024. Adsorption of SB (III) and PB(II) in wastewater by magnetic γ-Fe2O3-loaded sludge biochar: performance and mechanisms. Chemosphere 349, 140914. https://doi.org/10.1016/j.chemosphere.2023.140914.

Dhyani, V., Bhaskar, T., 2018. A comprehensive review on the pyrolysis of lignocellulosic biomass. Renew. Energy 129, 695–716. https://doi.org/10.1016/j.renene.2017.04.035.

Ding, Z., Wu, H., Hu, X., 2017. Multiple characterization for mechanistic insights of PB (II) sorption onto biochars derived from herbaceous plant, biosolid, and livestock waste. BioResources 12 (3), 6763–6772. https://doi.org/10.15376/biores.12.3.6763-6772.

Duwiejuah, A.-A.-O., Abubakari, A.-A.-O., Quainoo, A.K., Amadu, Y.-A.-O., 2020. Review of biochar properties and remediation of metal pollution of water and soil. Journal of Health and Pollution(2156–9614 (electronic)) 10 (27), 200902. https://doi.org/10.5696/2156-9614-10.27.200902.

Fan, S., Wang, Y., Li, Y., Wang, Z., Xie, Z., Tang, J., 2018. Removal of tetracycline from aqueous solution by biochar derived from rice straw. Environ. Sci. Pollut. Res. Int. 25 (29), 29529–29540. https://doi.org/10.1007/s11356-018-2976-0.

Fristak, V., Bosanska, D., Pipiska, M., Duriska, L., Bell, S.M., Soja, G., 2022. Physicochemical characterization of cherry pits-derived biochar. Materials (basel) 15 (2). https://doi.org/10.3390/ma15020408.

Gabhi, R., Basile, L., Kirk, D.W., Giorcelli, M., Tagliaferro, A., Jia, C.Q., 2020. Electrical conductivity of wood biochar monoliths and its dependence on pyrolysis temperature. Biochar 2 (3), 369–378. https://doi.org/10.1007/s42773-020-00056-0.

Gao, R., Fu, Q., Hu, H., Wang, Q., Liu, Y., Zhu, J., 2019. Highly-effective removal of pb by co-pyrolysis biochar derived from rape straw and orthophosphate. J. Hazard. Mater. 371, 191–197. https://doi.org/10.1016/j.jhazmat.2019.02.079.

Ghorbani, M., Konvalina, P., Walkiewicz, A., Neugschwandtner, R.W., Kopecky, M., Zamanian, K., Chen, W.H., Bucur, D., 2022. Feasibility of biochar derived from sewage sludge to promote sustainable agriculture and mitigate GHG emissions-a review. Int. J. Environ. Res. Public Health 19 (19). https://doi.org/10.3390/ijerph191912983.

Gonzalez-Canche, N.G., Carrillo, J.G., Escobar-Morales, B., Salgado-Transito, I., Pacheco, N., Pech-Cohuo, S.C., Pena-Cruz, M.I., 2021. Physicochemical and optical characterization of Citrus aurantium derived biochar for solar absorber applications. Materials (basel) 14 (16). https://doi.org/10.3390/ma14164756.

Herath, A., Layne, C.A., Perez, F., Hassan, E.I.B., Pittman, C.U., Mlsna, T.E., 2021. KOH-activated high surface area Douglas fir biochar for adsorbing aqueous CR(VI), PB(II) and CD(II). Chemosphere 269. https://doi.org/10.1016/j.chemosphere.2020.128409.

Hossain, M.K., Strezov, V., Chan, K.Y., Ziolkowski, A., Nelson, P.F., 2011. Influence of pyrolysis temperature on production and nutrient properties of wastewater sludge biochar. J. Environ. Manage. 92 (1), 223–228. https://doi.org/10.1016/j.jenvman.2010.09.008.

Hou, X., Deng, Y., Li, S., Fu, H., Dai, M., Jiang, X., Peng, C., 2022. Migration and transformation of heavy metals in chinese medicine residues during the process of traditional pyrolysis and solar pyrolysis. Chemosphere 293, 133658. https://doi.org/10.1016/j.chemosphere.2022.133658.

Hu, R., Xiao, J., Wang, T., Chen, G., Chen, L., Tian, X., 2020. Engineering of phosphate-functionalized biochars with highly developed surface area and porosity for efficient and selective extraction of uranium. Chem. Eng. J. 379 https://doi.org/10.1016/j.cej.2019.122388.

Huang, W.H., Chang, Y.J., Wu, R.M., Chang, J.S., Chuang, X.Y., Lee, D.J., 2023. Type-wide biochars loaded with Mg/Al layered double hydroxide as adsorbent for phosphate and mixed heavy metal ions in water. Environ. Res. 224, 115520 https://doi.org/10.1016/j.envres.2023.115520.

Ilic, M., Haegel, F.H., Lolic, A., Nedic, Z., Tosti, T., Ignjatovic, I.S., Linden, A., Jablonowski, N.D., Hartmann, H., 2022. Surface functional groups and degree of carbonization of selected chars from different processes and feedstock. PLoS One 17 (11), e0277365.

Ippolito, J.A., Cui, L., Kammann, C., Wrage-Mönnig, N., Estavillo, J.M., Fuertes-Mendizabal, T., Cayuela, M.L., Sigua, G., Novak, J., Spokas, K., Borchard, N., 2020. Feedstock choice, pyrolysis temperature and type influence biochar characteristics: a comprehensive meta-data analysis review. Biochar 2 (4), 421–438. https://doi.org/10.1007/s42773-020-00067-x.

Jiang, S., Yan, L., Wang, R., Li, G., Rao, P., Ju, M., Jian, L., Guo, X., Che, L., 2022. Recyclable nitrogen-doped biochar via low-temperature pyrolysis for enhanced LEAD(II) removal. Chemosphere 286 (Pt 1), 131666. https://doi.org/10.1016/j.chemosphere.2021.131666.

Jin, J., Li, Y., Zhang, J., Wu, S., Cao, Y., Liang, P., Zhang, J., Wong, M.H., Wang, M., Shan, S., Christie, P., 2016. Influence of pyrolysis temperature on properties and environmental safety of heavy metals in biochars derived from municipal sewage sludge. J. Hazard. Mater. 320, 417–426. https://doi.org/10.1016/j.jhazmat.2016.08.050.

Kalina, M., Sovova, S., Svec, J., Trudicova, M., Hajzler, J., Kubikova, L., Enev, V., 2022. The effect of pyrolysis temperature and the source biomass on the properties of biochar produced for the agronomical applications as the soil conditioner. Materials (basel) 15 (24). https://doi.org/10.3390/ma15248855.

Kaur, P., Sharma, N., Kaur, K., 2023. Influence of pyrolysis temperature on rice straw biochar properties and corresponding effects on dynamic changes in bispyribac-sodium adsorption and leaching behavior in soil. Pedosphere 33 (3), 463–478. https://doi.org/10.1016/j.pedsph.2022.06.046.

Kim, J., Kim, C., Park, M., Hwang, W., Kim, M., Hyun, S., 2021. Sorption of anthracene (C14H10) and 9-anthroic acid (C15H10O2) onto biochar-amended soils as affected by field aging treatments. Chemosphere 273. https://doi.org/10.1016/j.chemosphere.2021.129670.

Komkiene, J., Baltrenaite, E., 2015. Biochar as adsorbent for removal of heavy metal ions [CADMIUM(II), COPPER(II), LEAD(II), ZINC(II)] from aqueous phase. Int. J. Environ. Sci. Technol. 13 (2), 471–482. https://doi.org/10.1007/s13762-015-0873-3.

Laird, D.A., Fleming, P., Davis, D.D., Horton, R., Wang, B., Karlen, D.L., 2010. Impact of biochar amendments on the quality of a typical midwestern agricultural soil. Geoderma 158 (3–4), 443–449. https://doi.org/10.1016/j.geoderma.2010.05.013.

Li, H., Dong, X., da Silva, E.B., de Oliveira, L.M., Chen, Y., Ma, L.Q., 2017. Mechanisms of metal sorption by biochars: biochar characteristics and modifications. Chemosphere 178, 466–478. https://doi.org/10.1016/j.chemosphere.2017.03.072.

Li, H., Jiang, Q., Zhang, J., Wang, Y., Zhang, Y., 2022. Synchronization adsorption of Pb (II) and Ce(III) by biochar supported phosphate-doped ferrihydrite in aqueous solution: adsorption efficiency and mechanisms. Colloids Surf A Physicochem Eng Asp 648. https://doi.org/10.1016/j.colsurfa.2022.129230.

Li, Y., Wang, X., Li, J., Wang, Y., Song, J., Xia, S., Jing, H., Zhao, J., 2019b. Effects of struvite-humic acid loaded biochar/bentonite composite amendment on ZN(II) and antibiotic resistance genes in manure-soil. Chem. Eng. J. 375 https://doi.org/10.1016/j.cej.2019.122013.

Li, Y., Wang, F., Miao, Y., Mai, Y., Li, H., Chen, X., Chen, J., 2020. A lignin-biochar with high oxygen-containing groups for adsorbing lead ion prepared by simultaneous oxidization and carbonization. Bioresour. Technol. 307, 123165 https://doi.org/10.1016/j.biortech.2020.123165.

Li, J., Zheng, L., Wang, S.L., Wu, Z., Wu, W., Niazi, N.K., Shaheen, S.M., Rinklebe, J., Bolan, N., Ok, Y.S., Wang, H., 2019a. Sorption mechanisms of lead on silicon-rich biochar in aqueous solution: spectroscopic investigation. Sci. Total Environ. 672, 572–582. https://doi.org/10.1016/j.scitotenv.2019.04.003.

Liang, L., Xi, F., Tan, W., Meng, X., Hu, B., Wang, X., 2021. Review of Organic and Inorganic Pollutants Removal by Biochar and Biochar-Based Composites. Biochar(3), 255–281. https://doi.org/10.1007/s42773-021-00101-6.

Lin, H., Yang, D., Zhang, C., Liu, W., Zhang, L., Dong, Y., 2023a. Selective removal behavior of lead and cadmium from calcium-rich solution by MgO loaded soybean straw biochars and mechanism analysis. Chemosphere 319, 138010. https://doi.org/10.1016/j.chemosphere.2023.138010.

Lin, W., Zhou, J., Sun, S., 2023b. Cadmium and lead removal by Mg/Fe bimetallic oxide-loaded sludge-derived biochar: batch adsorption, kinetics, and mechanism. Environ. Sci. Pollut. Res. Int. https://doi.org/10.1007/s11356-023-28574-x.

Liu, X., Wen, J., Jiao, Y., Wang, Y., 2022. Determination of cellulose, hemicellulose and lignin content in abandoned fruit Core Shell. Journal of Yulin University 32 (02), 6–9. https://doi.org/10.16752/j.cnki.jylu.2022.02.002.

Liu, Y., n., Guo, Z. h., Sun, Y., Shi, W., Han, Z. y., Xiao, X. y., & Zeng, P, 2017. Stabilization of heavy metals in biochar pyrolyzed from phytoremediated giant reed (Arundo donax) biomass. Trans. Nonferrous Met. Soc. Chin. 27 (3), 656–665. https://doi.org/10.1016/s1003-6326(17)60073-6.

Lu, Q., Li, C., 2021. Comprehensive utilization of chinese medicine residues for industry and environment protection: turning waste into treasure. J. Clean. Prod. 279 https://doi.org/10.1016/j.jclepro.2020.123856.

Lu, H., Zhang, W., Wang, S., Zhuang, L., Yang, Y., Qiu, R., 2013. Characterization of sewage sludge-derived biochars from different feedstocks and pyrolysis temperatures. J. Anal. Appl. Pyrol. 102, 137–143. https://doi.org/10.1016/j.jaap.2013.03.004.

Ma, Q., Song, W., Wang, R., Zou, J., Yang, R., Zhang, S., 2018. Physicochemical properties of biochar derived from anaerobically digested dairy manure. Waste Manag. 79, 729–734. https://doi.org/10.1016/j.wasman.2018.08.023.

Manoharan, T., Ganeshalingam, S., Nadarajah, K., 2022. Mechanisms of emerging contaminants removal by novel neem chip biochar. Environmental Advances 7. https://doi.org/10.1016/j.envadv.2021.100158.

Marzeddu, S., Decima, M.A., Camilli, L., Bracciale, M.P., Genova, V., Paglia, L., Marra, F., Damizia, M., Stoller, M., Chiavola, A., Boni, M.R., 2022. Physical-chemical characterization of different carbon-based sorbents for environmental applications. Materials (basel) 15 (20). https://doi.org/10.3390/ma15207162.

Mazarji, M., Bayero, M.T., Minkina, T., Sushkova, S., Mandzhieva, S., Bauer, T.V., Soldatov, A., Sillanpää, M., Wong, M.H., 2023. Nanomaterials in biochar: review of their effectiveness in remediating heavy metal-contaminated soils. Sci. Total Environ. 880 https://doi.org/10.1016/j.scitotenv.2023.163330.

Mehmood, S., Ahmed, W., Alatalo, J.M., Mahmood, M., Imtiaz, M., Ditta, A., Ali, E.F., Abdelrahman, H., Slany, M., Antoniadis, V., Rinklebe, J., Shaheen, S.M., Li, W., 2022. Herbal plants- and rice straw-derived biochars reduced metal mobilization in fishpond sediments and improved their potential as fertilizers. Sci. Total Environ. 826, 154043 https://doi.org/10.1016/j.scitotenv.2022.154043.

Mohamed, B.A., Ellis, N., Kim, C.S., Bi, X., 2017. The role of tailored biochar in increasing plant growth, and reducing bioavailability, phytotoxicity, and uptake of heavy metals in contaminated soil. Environ. Pollut. 230, 329–338. https://doi.org/10.1016/j.envpol.2017.06.075.

Mukome, F.N., Zhang, X., Silva, L.C., Six, J., Parikh, S.J., 2013. Use of chemical and physical characteristics to investigate trends in biochar feedstocks. J. Agric. Food Chem. 61 (9), 2196–2204. https://doi.org/10.1021/jf3049142.

Regmi, P., Garcia Moscoso, J.L., Kumar, S., Cao, X., Mao, J., Schafran, G., 2012. Removal of copper and cadmium from aqueous solution using switchgrass biochar produced via hydrothermal carbonization process. J. Environ. Manage. 109, 61–69. https://doi.org/10.1016/j.jenvman.2012.04.047.

S, r., & p, b., 2019. The potential of lignocellulosic biomass precursors for biochar production: performance, mechanism and wastewater application—a review. Ind. Crop. Prod. 128, 405–423. https://doi.org/10.1016/j.indcrop.2018.11.041.

Shao, F., Zhang, X., Sun, X., Shang, J., 2021. Antibiotic removal by activated biochar: performance, isotherm, and kinetic studies. J. Dispers. Sci. Technol. 42 (9), 1274–1285. https://doi.org/10.1080/01932691.2020.1737106.

Shen, B., Li, G., Wang, F., Wang, Y., He, C., Zhang, M., Singh, S., 2015. Elemental mercury removal by the modified bio-char from medicinal residues. Chem. Eng. J. (amsterdam Neth.), 272, 28–37. https://doi.org/10.1016/j.cej.2015.03.006.

Shi, R.Y., Ni, N., Nkoh, J.N., Li, J.Y., Xu, R.K., Qian, W., 2019. Beneficial dual role of biochars in inhibiting soil acidification resulting from nitrification. Chemosphere 234, 43–51. https://doi.org/10.1016/j.chemosphere.2019.06.030.

Song, B., Chen, M., Zhao, L., Qiu, H., Cao, X., 2019. Physicochemical property and colloidal stability of micron- and nano-particle biochar derived from a variety of feedstock sources. Sci. Total Environ. 661, 685–695. https://doi.org/10.1016/j.scitotenv.2019.01.193.

Su, X., Xue, Q., Sun, M., Liu, J., Wong, M.H., Wang, C., Chen, S., 2021. Co-production of polysaccharides, ginsenosides and succinic acid from Panax ginseng residue: a typical industrial herbal waste. Bioresour. Technol. 331, 125073 https://doi.org/10.1016/j.biortech.2021.125073.

Sui, F., Jiao, M., Kang, Y., Joseph, S., Li, L., Bian, R., Munroe, P., Mitchell, D.R.G., Pan, G., 2021. Investigating the cadmium adsorption capacities of crop straw biochars produced using various feedstocks and pyrolysis temperatures. Environ. Sci. Pollut. Res. 28 (17), 21516–21527. https://doi.org/10.1007/s11356-020-11979-3.

Tao, W., Jin, J., Zheng, Y., Li, S., 2021. Current advances of resource utilization of herbal extraction residues in China. Waste Biomass Valoriz. 12 (11), 5853–5868. https://doi.org/10.1007/s12649-021-01428-8.

Tian, S., Gong, X., Yu, Q., Yao, F., Li, W., Guo, Z., Zhang, X., Yuan, Y., Fan, Y., Bian, R., Wang, Y., Zhang, X., Li, L., Pan, G., 2023. Efficient removal of CD(II) and PB(II) from aqueous solution using biochars derived from food waste. Environ. Sci. Pollut. Res. 30 (58), 122364–122380. https://doi.org/10.1007/s11356-023-30777-1.

Tran, H.N., You, S.J., Chao, H.P., 2016. Effect of pyrolysis temperatures and times on the adsorption of cadmium onto orange peel derived biochar. Waste Manag. Res. 34 (2), 129–138. https://doi.org/10.1177/0734242X15615698.

Wang, S., Gao, B., Zimmerman, A.R., Li, Y., Ma, L., Harris, W.G., Migliaccio, K.W., 2015. Physicochemical and sorptive properties of biochars derived from woody and herbaceous biomass. Chemosphere 134, 257–262. https://doi.org/10.1016/j.chemosphere.2015.04.062.

Wang, S., Li, X., Zhu, Y., 2023. Comparison of the adsorption capacity and mechanisms of mixed heavy metals in wastewater by sheep manure biochar and Robinia pseudoacacia biochar. Water Sci. Technol. 87 (12), 3083–3094. https://doi.org/10.2166/wst.2023.180.

Wang, J., Liang, Q., Chen, J., Liu, Z., 2019. Rapid determination of lignin content in agricultural wastes. Cement Engineering(04), 76–77. https://doi.org/10.13697/j.cnki.32-1449/tu.2019.04.026.

Wang, T., Liao, Q., Wu, Y., Wang, X., Fu, C., Geng, F., Qu, Y., Zhang, J., 2020. A composite hydrogel loading natural polysaccharides derived from Periplaneta Americana herbal residue for diabetic wound healing. Int. J. Biol. Macromol. 164, 3846–3857. https://doi.org/10.1016/j.ijbiomac.2020.08.156.

Wang, J., Shi, L., Zhai, L., Zhang, H., Wang, S., Zou, J., Shen, Z., Lian, C., Chen, Y., 2021. Analysis of the long-term effectiveness of biochar immobilization remediation on heavy metal contaminated soil and the potential environmental factors weakening the remediation effect: a review. Ecotoxicol. Environ. Saf. 207, 111261 https://doi.org/10.1016/j.ecoenv.2020.111261.

Wei, L., Huang, Y., Huang, L., Li, Y., Huang, Q., Xu, G., Muller, K., Wang, H., Ok, Y.S., Liu, Z., 2020. The ratio of H/C is a useful parameter to predict adsorption of the herbicide metolachlor to biochars. Environ. Res. 184, 109324 https://doi.org/10.1016/j.envres.2020.109324.

Wu, H., Che, X., Ding, Z., Hu, X., Creamer, A.E., Chen, H., Gao, B., 2016. Release of soluble elements from biochars derived from various biomass feedstocks. Environ. Sci. Pollut. Res. 23 (2), 1905–1915. https://doi.org/10.1007/s11356-015-5451-1.

Wu, D., Lu, J., Wu, J., Li, B., 2023. To explore the remediation mechanism and effect of biochar and KH2PO4 on soils contaminated with heavy metal ions Hg2+, Cd2+ and Pb2+. J. Environ. Sci. Health A 1–13. https://doi.org/10.1080/10934529.2023.2290421.

Xi, Y., Liu, Y., Ye, X., Du, J., Kong, X., Guo, D., Xiao, Q., 2021. Enhanced anaerobic biogas production from wheat straw by herbal-extraction process residues supplementation. Front. Bioeng. Biotechnol. 9, 623594 https://doi.org/10.3389/fbioe.2021.623594.

Xiao, H., Lin, Q., Li, G., Zhao, X., Li, J., Li, E., 2022. Comparison of biochar properties from 5 kinds of halophyte produced by slow pyrolysis at 500 °C. Biochar 4 (1). https://doi.org/10.1007/s42773-022-00141-6.

Yaashikaa, P.R., Senthil Kumar, P., Varjani, S.J., Saravanan, A., 2019. Advances in production and application of biochar from lignocellulosic feedstocks for remediation of environmental pollutants. Bioresour. Technol. 292, 122030 https://doi.org/10.1016/j.biortech.2019.122030.

Yang, F., Lv, J., Zhou, Y., Wu, S., Sima, J., 2023. Co-pyrolysis of biomass and phosphate tailing to produce potential phosphorus-rich biochar: efficient removal of heavy metals and the underlying mechanisms. Environ. Sci. Pollut. Res. Int. 30 (7), 17804–17816. https://doi.org/10.1007/s11356-022-23128-z.

Yu, J., Deem, L.M., Crow, S.E., Deenik, J., Penton, C.R., 2019. Comparative metagenomics reveals enhanced nutrient cycling potential after 2 years of biochar amendment in a tropical oxisol. Appl. Environ. Microbiol. 85 (11) https://doi.org/10.1128/AEM.02957-18.

Yu, M., He, D., Zhang, Y., He, D., Wang, X., Zhou, J., 2021a. Characterization of lignin extracted from Acanthopanax senticosus residue using different methods on UV-resistant behavior. Int. J. Biol. Macromol. 192, 498–505. https://doi.org/10.1016/j.ijbiomac.2021.09.182.

Yu, W., Hu, J., Yu, Y., Ma, D., Gong, W., Qiu, H., Hu, Z., Gao, H.W., 2021b. Facile preparation of sulfonated biochar for highly efficient removal of toxic PB(II) and CD (II) from wastewater. Sci. Total Environ. 750, 141545 https://doi.org/10.1016/j.scitotenv.2020.141545.

Yuan, T., Zhang, S., Chen, Y., Zhang, R., Chen, L., Ruan, X., Zhang, S., Zhang, F., 2021. Enhanced reactive blue 4 biodegradation performance of newly isolated white rot fungus antrodia P5 by the synergistic effect of herbal extraction residue. Front. Microbiol. 12, 644679 https://doi.org/10.3389/fmicb.2021.644679.

Zhang, J., Huang, B., Chen, L., Li, Y., Li, W., Luo, Z., 2018. Characteristics of biochar produced from yak manure at different pyrolysis temperatures and its effects on the yield and growth of highland barley. Chem. Spec. Bioavailab. 30 (1), 57–67. https://doi.org/10.1080/09542299.2018.1487774.

Zhang, Q., Zhang, D., Lu, W., Khan, M.U., Xu, H., Yi, W., Lei, H., Huo, E., Qian, M., Zhao, Y., Zou, R., 2020. Production of high-density polyethylene biocomposites from rice husk biochar: effects of varying pyrolysis temperature. Sci. Total Environ. 738, 139910 https://doi.org/10.1016/j.scitotenv.2020.139910.

Zhao, H., Li, X., Zhang, L., Hu, Z., Zhong, L., Xue, J., 2021. Preparation and bacteriostatic research of porous polyvinyl alcohol / biochar / nanosilver polymer gel for drinking water treatment. Sci. Rep. 11 (1), 12205. https://doi.org/10.1038/s41598-021-91833-9.

Zhao, F., Tang, L., Jiang, H., Mao, Y., Song, W., Chen, H., 2023. Prediction of heavy metals adsorption by hydrochars and identification of critical factors using machine learning algorithms. Bioresour. Technol. 383, 129223 https://doi.org/10.1016/j.biortech.2023.129223.

Zheng, T., Ouyang, S., Zhou, Q., 2023. Synthesis, characterization, safety design, and application of NPs@BC for contaminated soil remediation and sustainable agriculture. Biochar 5 (1). https://doi.org/10.1007/s42773-022-00198-3.

Zhou, G., Luo, J., Liu, C., Chu, L., Crittenden, J., 2018a. Efficient heavy metal removal from industrial melting effluent using fixed-bed process based on porous hydrogel adsorbents. Water Res. 131, 246–254. https://doi.org/10.1016/j.watres.2017.12.067.

Zhou, Y., Selvam, A., Wong, J.W.C., 2018b. Chinese medicinal herbal residues as a bulking agent for food waste composting. Bioresour. Technol. 249, 182–188. https://doi.org/10.1016/j.biortech.2017.09.212.

Zhou, Y., Qin, S., Verma, S., Sar, T., Sarsaiya, S., Ravindran, B., Liu, T., Sindhu, R., Patel, A.K., Binod, P., Varjani, S., Rani Singhnia, R., Zhang, Z., Awasthi, M.K., 2021c. Production and beneficial impact of biochar for environmental application: a comprehensive review. Bioresour. Technol. 337, 125451 https://doi.org/10.1016/j.biortech.2021.125451.

Zhou, Y., Lan, Y., Short, M.D., Shi, J., Zhang, Q., Xu, J., Qian, G., 2023. Effective use of sugarcane-bagasse-derived KOH-activated biochar for remediating norfloxacin-contaminated water. Toxics 11 (11). https://doi.org/10.3390/toxics11110908.

Zhou, C., Song, X., Wang, Y., Wang, H., Ge, S., 2022. The sorption and short-term immobilization of lead and cadmium by nano-hydroxyapatite/biochar in aqueous solution and soil. Chemosphere 286 (Part_3), 131810. https://doi.org/10.1016/j.chemosphere.2021.131810.

Zhou, X.Y., Xie, F., Jiang, M., Ke-Ao, L., Tian, S.G., 2021b. Physicochemical properties and lead ion adsorption of biochar prepared from turkish gall residue at different pyrolysis temperatures. Microsc. Res. Tech. 84 (5), 1003–1011. https://doi.org/10.1002/jemt.23661.

Zhou, M., Yang, X., Sun, R., Wang, X., Yin, W., Wang, S., Wang, J., 2021a. The contribution of lignocellulosic constituents to CR(VI) reduction capacity of biochar-supported zerovalent iron. Chemosphere 263. https://doi.org/10.1016/j.chemosphere.2020.127871.